The Astronomical Journal, 168:93 (24pp), 2024 August https://doi.org/10.3847/1538-3881/ad55ea

TOI-2015 b: A Warm Neptune with Transit Timing Variations Orbiting an Active Mid-type M Dwarf

Sinclaire E. Jones[1,2], Guðmundur Stefánsson[2,3,30], Kento Masuda[4], Jessica E. Libby-Roberts[5], Cristilyn N. Gardner[6], Rae Holcomb[7], Corey Beard[7,31], Paul Robertson[7], Caleb I. Cañas[8,32], Suvrath Mahadevan[5,9], Shubham Kanodia[10], Andrea S. J. Lin[5,9], Henry A. Kobulnicky[6], Brock A. Parker[6], Chad F. Bender[11], William D. Cochran[12,13], Scott A. Diddams[14,15,16], Rachel B. Fernandes[5,9,33], Arvind F. Gupta[5,9], Samuel Halverson[17], Suzanne L. Hawley[18], Fred R. Hearty[5,9], Leslie Hebb[19,20], Adam Kowalski[21,22,23], Jack Lubin[7], Andrew Monson[11], Joe P. Ninan[24], Lawrence Ramsey[5,9], Arpita Roy[25,26], Christian Schwab[27], Ryan C. Terrien[28], and John Wisniewski[29]
[1] Department of Astronomy, The Ohio State University, 4055 McPherson Laboratory, Columbus, OH 43210, USA
[2] Department of Astrophysical Sciences, Princeton University, 4 Ivy Lane, Princeton, NJ 08540, USA
[3] Anton Pannekoek Institute for Astronomy, University of Amsterdam, Science Park 904, 1098 XH Amsterdam, The Netherlands
[4] Department of Earth and Space Science, Graduate School of Science, Osaka University, 1-1 Machikaneyama, Toyonaka, Osaka 560-0043, Japan
[5] Department of Astronomy & Astrophysics, 525 Davey Laboratory, The Pennsylvania State University, University Park, PA 16802, USA
[6] Department of Physics & Astronomy, University of Wyoming, Laramie, WY 82070, USA
[7] Department of Physics & Astronomy, The University of California, Irvine, CA 92697, USA
[8] NASA Goddard Space Flight Center, 8800 Greenbelt Road, Greenbelt, MD 20771, USA
[9] Center for Exoplanets and Habitable Worlds, 525 Davey Laboratory, The Pennsylvania State University, University Park, PA 16802, USA
[10] Earth and Planets Laboratory, Carnegie Institution for Science, 5241 Broad Branch Road, NW, Washington, DC 20015, USA
[11] Steward Observatory, The University of Arizona, 933 N. Cherry Avenue, Tucson, AZ 85721, USA
[12] McDonald Observatory and Department of Astronomy, The University of Texas at Austin, 2515 Speedway, Austin, TX 78712, USA
[13] Center for Planetary Systems Habitability, The University of Texas at Austin, 2515 Speedway, Austin, TX 78712, USA
[14] Electrical, Computer & Energy Engineering, University of Colorado Boulder, 425 UCB, Boulder, CO 80309, USA
[15] Department of Physics, University of Colorado Boulder, 2000 Colorado Avenue, Boulder, CO 80309, USA
[16] National Institute of Standards and Technology, 325 Broadway, Boulder, CO 80305, USA
[17] Jet Propulsion Laboratory, California Institute of Technology, 4800 Oak Grove Drive, Pasadena, CA 91109, USA
[18] Astronomy Department, University of Washington, Seattle, WA 98195, USA
[19] Department of Physics, Hobart and William Smith Colleges, 300 Pulteney Street, Geneva, NY 14456, USA
[20] Department of Astronomy, Cornell University, 245 East Avenue, Ithaca, NY 14850, USA
[21] Department of Astrophysical and Planetary Sciences, University of Colorado Boulder, 2000 Colorado Avenue, Boulder, CO 80305, USA
[22] National Solar Observatory, University of Colorado Boulder, 3665 Discovery Drive, Boulder, CO 80303, USA
[23] Laboratory for Atmospheric and Space Physics, University of Colorado Boulder, 3665 Discovery Drive, Boulder, CO 80303, USA
[24] Department of Astronomy and Astrophysics, Tata Institute of Fundamental Research, Homi Bhabha Road, Colaba, Mumbai 400005, India
[25] Space Telescope Science Institute, 3700 San Martin Drive, Baltimore, MD 21218, USA
[26] Department of Physics and Astronomy, Johns Hopkins University, 3400 N Charles Street, Baltimore, MD 21218, USA
[27] School of Mathematical and Physical Sciences, Macquarie University, Balaclava Road, North Ryde, NSW 2109, Australia
[28] Carleton College, One North College Street, Northfield, MN 55057, USA
[29] NASA Headquarters, 300 Hidden Figures Way SW, Washington DC 20546, USA
Received 2023 October 17; revised 2024 May 3; accepted 2024 May 9; published 2024 July 26

Abstract

We report the discovery of a close-in ($P_{\rm orb} = 3.349$ days) warm Neptune with clear transit timing variations (TTVs) orbiting the nearby ($d = 47.3$ pc) active M4 star, TOI-2015. We characterize the planet's properties using Transiting Exoplanet Survey Satellite (TESS) photometry, precise near-infrared radial velocities (RVs) with the Habitable-zone Planet Finder Spectrograph, ground-based photometry, and high-contrast imaging. A joint photometry and RV fit yields a radius $R_p = 3.37^{+0.15}_{-0.20}\,R_\oplus$, mass $m_p = 16.4^{+4.1}_{-4.1}\,M_\oplus$, and density $\rho_p = 2.32^{+0.38}_{-0.37}$ g cm^{-3} for TOI-2015 b, suggesting a likely volatile-rich planet. The young, active host star has a rotation period of $P_{\rm rot} = 8.7 \pm 0.9$ days and associated rotation-based age estimate of 1.1 ± 0.1 Gyr. Though no other transiting planets are seen in the TESS data, the system shows clear TTVs of super-period $P_{\rm sup} \approx 430$ days and amplitude $\sim$100 minutes. After considering multiple likely period-ratio models, we show an outer planet candidate near a 2:1 resonance can explain the observed TTVs while offering a dynamically stable solution. However, other possible two-planet solutions—including 3:2 and 4:3 resonances—cannot be conclusively excluded without further observations. Assuming a 2:1 resonance in the joint TTV-RV modeling suggests a mass of $m_b = 13.3^{+4.7}_{-4.5}\,M_\oplus$ for TOI-2015 b and $m_c = 6.8^{+3.5}_{-2.3}\,M_\oplus$ for the outer candidate. Additional transit and RV

[30] NASA Sagan Fellow.
[31] NASA FINESST Fellow.
[32] NASA Postdoctoral Fellow.
[33] President's Postdoctoral Fellow.

observations will be beneficial to explicitly identify the resonance and further characterize the properties of the system.

Unified Astronomy Thesaurus concepts: Exoplanets (498); M dwarf stars (982); Transits (1711); Radial velocity (1332); Transit timing variation method (1710)

Materials only available in the online version of record: data behind figure, machine-readable tables

1. Introduction

M dwarfs are the most common type of star in the Milky Way galaxy and the lowest-mass spectral type on the main sequence (Henry et al. 2006). These low masses ($0.075\,M_{\odot} < M_{*} < 0.6\,M_{\odot}$) make M dwarfs ideal hosts for planet detection and in-depth characterization. Based on results from the Kepler mission, we know that M dwarfs tend to host more small planets on short-period orbits than hotter, more massive stars (Dressing & Charbonneau 2015; Muirhead et al. 2015; Hardegree-Ullman et al. 2019). However, because the Kepler mission observed a fixed field with a focus on FGK stars, it was only able to detect a limited number of M-dwarf planets.

Both the K2 mission (Howell et al. 2014) and the Transiting Exoplanet Survey Satellite mission (TESS; Ricker et al. 2015) have sampled a different population of planet hosts than Kepler, including many nearby M dwarfs. In particular, with its red-optimized bandpass and all-sky coverage, TESS is particularly sensitive to planets orbiting nearby M dwarfs, having already detected hundreds of planetary candidates orbiting these cooler stars, which yield further insights into the population of planets orbiting nearby M stars (e.g., Bryant et al. 2023; Gan et al. 2023; Ment & Charbonneau 2023).

Among the diverse demographics of exoplanets, multiplanet systems are especially interesting targets, as we can extract valuable clues to their formation from their orbital architectures. For instance, when planets are at or near orbital resonances, we may see evidence of transit timing variations (TTVs; Agol et al. 2005; Holman & Murray 2005)—deviations from strictly periodic transits due to gravitational interactions between planets. Measured TTVs can be used to detect additional planets in the system and constrain their eccentricities and masses. It is theorized that TTV systems could have formed through convergent migration of planets while still embedded in a viscous protoplanetary disk (e.g., Masset & Snellgrove 2001; Snellgrove et al. 2001; Cresswell & Nelson 2006).

Currently, there are about 150 confirmed TTV systems, only ~10 of which have M-dwarf hosts. Notable examples of M-dwarf TTV systems include the well-studied TRAPPIST-1 system (Gillon et al. 2016, 2017), a system of seven transiting terrestrial planets in a resonant chain, and AU Mic, a young, active nearby M star with two transiting Neptunes (Plavchan et al. 2020; Martioli et al. 2021). There are also TTV systems that contain both transiting and nontransiting planets. For instance, K2-146 is a system of two resonant sub-Neptunes in which the initially nontransiting planet c precessed into view over time (Hirano et al. 2018; Hamann et al. 2019; Lam et al. 2020). Additionally, there is KOI-142, whose sub-Neptune has 12 hr TTVs (Nesvorný et al. 2013). An outer planet near 2:1 resonance was later confirmed in this system via radial velocity (RV) follow-up observations (Barros et al. 2014).

Here we report on the discovery of a close-in ($P_{\rm orb} =$ 3.349 days) warm Neptune with clear TTVs transiting the nearby ($d = 47.3$ pc) active mid-type M dwarf TOI-2015. We confirm the planetary nature of the transiting object using TESS photometry along with ground-based photometric observations, high-contrast imaging, and precise RV observations. Photometry from TESS and ground-based instruments displays clear evidence of TTVs with a super-period of $P_{\rm sup} \approx 430$ days and an amplitude of ~100 minutes. However, the two sectors of TESS data reveal no significant evidence of additional transiting planets in the system. We constrain the mass of TOI-2015 b using precise near-infrared (NIR) RVs obtained with the Habitable-zone Planet Finder (HPF; Mahadevan et al. 2012, 2014) on the 10 m Hobby–Eberly Telescope along with a joint TTV and RV fit assuming likely period ratios of the system.

This paper is organized as follows. Section 2 describes the observations and data reduction. In Section 3, we report the key parameters of the host star. Section 4 provides an in-depth look at the transit, RV, and TTV modeling and the resulting planet parameter constraints. In Section 5, we place TOI-2015 in context with other M dwarfs and multiplanet systems with detectable TTVs. We conclude in Section 6 with a summary of our key findings.

2. Observations and Data Reduction

2.1. TESS Photometry

TOI-2015 is listed as TIC 368287008 in the TESS Input Catalog (Stassun et al. 2018, 2019), and is included in the mission's catalog of cool dwarf targets (Muirhead et al. 2018). TESS observed TOI-2015 with a 2 minutes cadence in two sectors: Sector 24, from 2020 April 16 to 2020 May 13, and Sector 51, from 2022 April 22 to 2022 May 18. Analysis of the light curve by the TESS Science Processing Operations Center (SPOC) identified a possible planetary signal, TOI-2015.01 (available on the TESS alerts website), where SPOC data validation reports note no significant centroid offsets during transit events (Twicken et al. 2018; Li et al. 2019).[34]

The TOI-2015 TESS photometry is displayed in Figure 1. We retrieved these data using the `lightkurve` package (Lightkurve Collaboration et al. 2018). For our photometric analysis, we used the presearch data conditioning single-aperture photometry (PDCSAP) light curve, which uses pixels chosen to maximize the signal-to-noise ratio (S/N) of the target and has removed systematic variability by fitting out trends common to many stars (Smith et al. 2012; Stumpe et al. 2014). Figure 2 highlights the TESS aperture of TOI-2015 ($T_{\rm mag} = 12.8$), along with two known nearby objects within 40″ as detected by Gaia: TIC 368287010 ($T_{\rm mag} = 13.0$; angular separation = 32″) and TIC 368287012 ($T_{\rm mag} = 16.5$; angular separation = 37″). From their separation and lower brightness than TOI-2015, the nearby stars result in a modest dilution of the TESS light curve with a contamination ratio of 0.131892 ± 0.001231. The flux contamination, which can be computed using the `tic_contam.py` script from Paegert et al. (2021), is corrected for in the PDCSAP light curves as prepared by SPOC.[35]

[34] https://tev.mit.edu/data/

[35] https://github.com/mpaegert/tic_inspect/blob/master/tic_contam.py

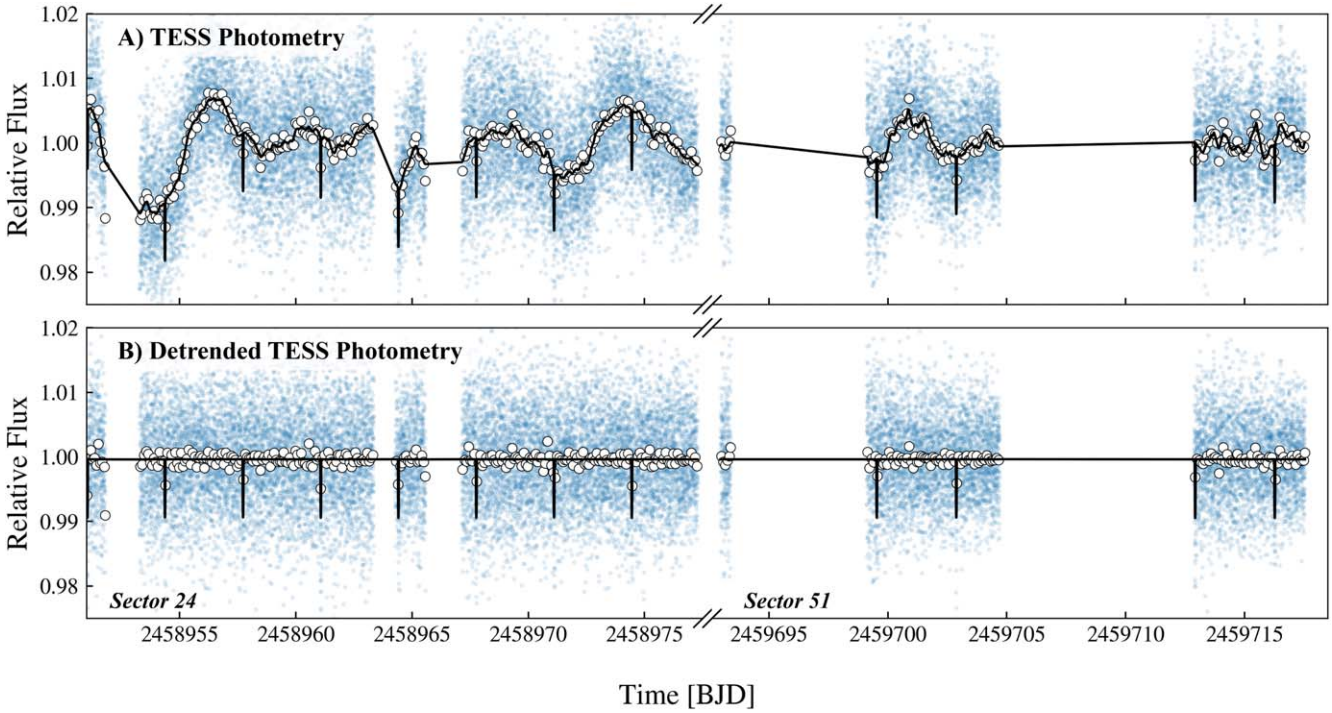

Figure 1. TESS photometry of TOI-2015 from Sectors 24 and 51. Blue points are the PDCSAP data, and white points show 2 hr binned data. (A) TESS photometry showing out-of-transit variability. The black curve shows the transit model along with the Gaussian process (GP) quasiperiodic correlated noise model from our `juliet` fit (black curve). (B) TESS photometry after removing out-of-phase variability as modeled by the GP. Transits of TOI-2015 b are clearly visible. The data behind this figure are available in machine-readable format. In addition to the TESS photometry, it also includes the photometry from the ARC, LCOGT, RBO, and WIRO data sets. The latter can be used to generate other figures in the article.

(The data used to create this figure are available in the online article.)

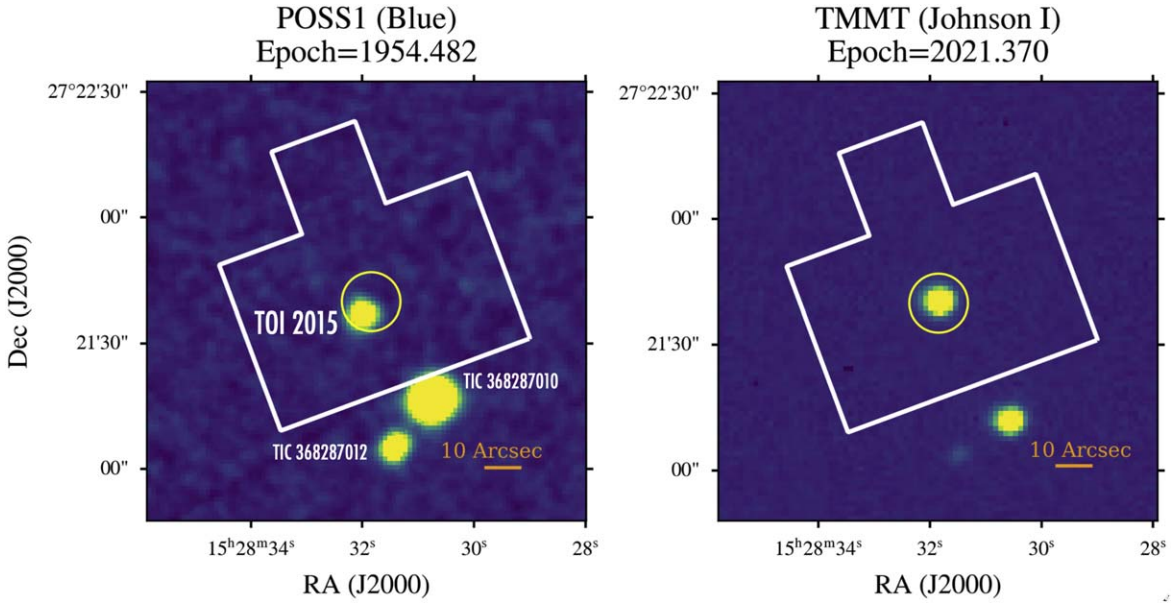

Figure 2. Seeing-limited imaging. Left: seeing-limited imaging from POSS-1 in the blue filter from the Digital Sky Survey-1 from 1954. Right: seeing-limited imaging obtained with TMMT in the Johnson *I* filter in 2021 May. The filled yellow circle (7″ radius) denotes the Gaia position of TOI-2015 at the Gaia epoch (2015.5). The white lines show the outline of the TESS aperture. North is up, and east is to the left. The two nearby stars, TIC 368287010 and TIC 368287012, result in a modest dilution of 0.131892 ± 0.001231 in the TESS aperture. No other nearby stars are detected.

2.2. Seeing-limited Imaging

To constrain blends within the TESS aperture, Figure 2 compares seeing-limited images of TOI-2015 observed in 1954 and 2021. The 1954 image was captured during the first Palomar Sky Survey (POSS-1), and we accessed these data with `astroquery skyview` (Ginsburg et al. 2018). In the more recent seeing-limited image, we observed TOI-2015 with the Three-hundred MilliMeter Telescope (TMMT; Monson et al. 2017) at Las Campanas Observatory on 2021 May 16. We obtained the TMMT image with the Johnson *I* filter and an

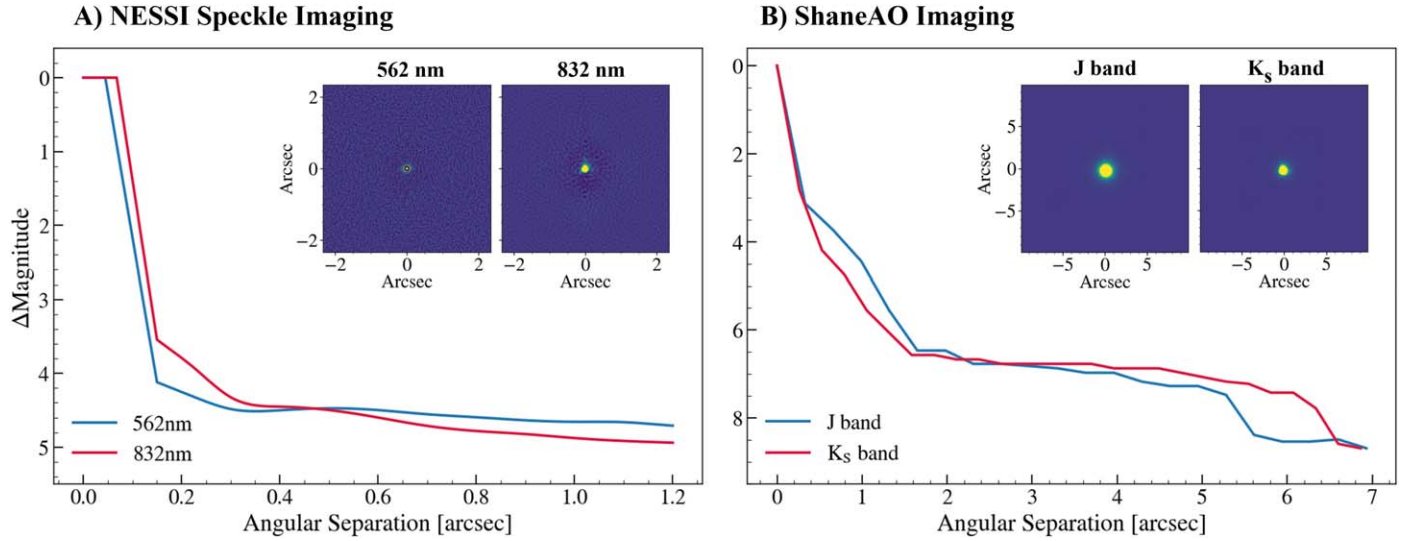

Figure 3. High-contrast imaging of TOI-2015 from (A) WYIN 3.5 m/NESSI speckle imaging, and (B) Lick 3 m/ShaneAO. The curves show azimuthally averaged radial Δ magnitude constraints, in the 562 nm (blue) and 832 nm (red) filters for NESSI, and the J and K_S band for ShaneAO. The inset images show the corresponding high-contrast images. We see no evidence of nearby companions in either the NESSI or the ShaneAO observations.

exposure time of 120 s. The nearby stars, TIC 368287010 ($T_{\rm mag} = 13.0$) and TIC 368287012 ($T_{\rm mag} = 16.5$), are highlighted in Figure 2. Due to TOI-2015's modest proper motion of $\mu_\alpha = -56$ mas yr^{-1} and $\mu_\delta = 64$ mas yr^{-1}, TOI-2015 has moved slightly from the POSS-1 epoch to the 2021 epoch. No background star is seen in the POSS-1 data at the current location of TOI-2015 that could be a significant source of dilution.

2.3. High-contrast Imaging with WIYN 3.5 m/NESSI and Lick 3 m/ShaneAO

We obtained speckle imaging of TOI-2015 on 2021 March 29 with the NASA Exoplanet Star and Speckle Imager (NESSI; Scott et al. 2018) on the WIYN 3.5 m telescope to determine if the transit signals could be explained by contamination from nearby stars and other false positives (e.g., background eclipsing binary).[36] The target was observed in narrowband filters centered around 562 and 832 nm. The data were reduced using the standard NESSI pipeline (Howell et al. 2011). The resulting contrast curves and their associated $4\farcs6 \times 4\farcs6$ images are displayed in Figure 3. We place a $\Delta{\rm mag} \sim 4.5$ limit on nearby objects between an angular separation of $0\farcs2$–$1\farcs2$ and identify no additional nearby sources.

Additionally, we observed TOI-2015 with high-contrast adaptive optics (AO) imaging with the ShaneAO system on the 3 m Telescope at Lick Observatory on 2021 May 27 (Gavel et al. 2014). This allows us to further discern potential transit false positives. We observed in the K_s and J bands with 60 s and 150 s exposures, respectively. The data were reduced following Stefansson et al. (2020a). These results are shown in Figure 3. We identify no nearby companions of $\Delta{\rm mag} \sim 7$ within a $1\farcs5$–$7''$ radius of TOI-2015.

2.4. Near-infrared RVs with the HET 10 m/HPF

The HPF (Mahadevan et al. 2012, 2014) is a NIR fiber-fed (Kanodia et al. 2018) spectrograph on the 10 m HET at McDonald Observatory in Texas. HPF covers the information-rich z, Y, and J bands (810–1280 nm) with a spectral resolution of $R \sim 55{,}000$. In order to achieve precise RV measurements, the instrument's optics are kept under high-quality vacuum at a constant operating temperature of ∼180 K with millikelvin long-term stability (Stefansson et al. 2016). All observations were executed within the HET queue (Shetrone et al. 2007). HPF has a laser frequency comb (LFC) calibrator that can provide ∼20 cm s^{-1} RV calibration precision in ∼10 minutes bins (Metcalf et al. 2019). Due to the faintness of the target, we followed Stefansson et al. (2020a); we did not use the simultaneous LFC in order to minimize the risk of contaminating the science spectrum from scattered light, and we extrapolated the wavelength solution from LFC calibration exposures that were taken throughout the night. This methodology has been shown to be precise at the ∼30 cm s^{-1} level, substantially smaller than the median photon-limited RV precision we obtain on TOI-2015.

In total, we obtained 109 HPF spectra in over 40 HET visits with 650 s exposures and a median S/N of ∼45 evaluated per 1D extracted pixel at 1 μm. There were five spectra that had a S/N < 17, which we removed from the analysis. The remaining 104 spectra were obtained in 37 HET visits, have a median S/N of 46, and span a baseline of 639 days. The spectra have a median unbinned RV uncertainty of 24 m s^{-1} and a nightly (2–3 visits per night) binned RV uncertainty of 15 m s^{-1}. We used the binned measurements for our RV analysis.

We extracted the HPF 1D spectra using the HPF pipeline, following the procedures in Kaplan et al. (2018), Ninan et al. (2018), and Metcalf et al. (2019). We extracted high-precision HPF RVs using a modified version of the spectrum radial velocity analyzer (`SERVAL`; Zechmeister et al. 2018) pipeline that we have optimized to extract RVs for HPF spectra, following the procedures in Stefansson et al. (2020a). `SERVAL` uses the template-matching technique to extract precise RVs for M dwarfs. To calculate barycentric corrections for the HPF spectra, we use the `barycorrpy` package (Kanodia & Wright 2018), which uses the methodology of Wright & Eastman (2014) to calculate barycentric velocities. We use the

[36] The WIYN Observatory is a joint facility of the University of Wisconsin-Madison, Indiana University, Purdue University, Penn State University, Princeton University, the NSF's National Optical-Infrared Astronomy Research Laboratory, and NASA.

10 HPF orders least affected by tellurics, covering the wavelength regions from 8540–8890, 9940–10940, and 12375–12525 Å. We subtracted the estimated sky background from the stellar spectrum using the dedicated HPF sky fiber. Following the methodology described in Metcalf et al. (2019) and Stefansson et al. (2020a), we explicitly masked out telluric lines and sky-emission lines to minimize their impact on the RV determination. Table 6 in Appendix B lists the RVs from HPF used in this work.

2.5. Ground-based Follow-up Photometry

2.5.1. LCOGT 1 m Photometry

A partial transit of TOI-2015 b was observed by the Las Cumbres Observatory Global Telescope (LCOGT) observing team on the night of 2020 July 4 using the Sinistro imaging cameras on the 1 m telescope at its South African Astronomical Observatory site (Brown et al. 2013). The Bessell *I* filter was used with an exposure time of 100 s. The imager uses 1×1 binning in its full-frame configuration with a gain of $10.3\,e^{-}\,ADU^{-1}$ and read noise of $7.6\,e^{-}$. The camera has a plate scale of $0\farcs389\,pix^{-1}$, with a field of view of $26\farcm5 \times 26\farcm5$. We accessed the data, processed using the BANZAI pipeline (McCully et al. 2018), through the publicly accessible LCOGT archive (Proposal ID: KEY2020B-005, PI: Shporer).[37]

We reduced the photometry using `AstroImageJ` (Collins et al. 2017), which accounts for photometric errors due to photon, read, dark, digitization, and background noise. In addition, we added the expected error due to scintillation following the methodology in Stefansson et al. (2017). After testing a number of different aperture sizes and reference stars, we converged on a final aperture radius of 10 pix with an inner sky background annulus of 16 pix and outer annulus of 24 pix, as this extraction provided the highest overall photometric precision.

2.5.2. Diffuser-assisted WIRO 2.3 m Photometry

We obtained a full transit of TOI-2015 b on the night of 2021 July 18 with the Wyoming Infrared Observatory (WIRO) DoublePrime prime-focus imager on the WIRO 2.3 m Telescope (Findlay et al. 2016). The images used the Sloan Digital Sky Survey (SDSS) i' filter and an exposure time of 75 s. In the 1×1 binning mode, the WIRO detector has a gain of $2.6\,e^{-}\,ADU^{-1}$ and a read noise of $5.2\,e^{-}$. The four-amplifier mode has a 20 s readout time. The plate scale is $0\farcs576\,pix^{-1}$, covering a field of view of $39' \times 39'$.

We used the Engineered Diffuser, a nanofabricated piece of optic able to mold the image of a star into a broad and stabilized shape, which can help provide high-precision photometry (Stefansson et al. 2017, 2018a, 2018b), available on the WIRO DoublePrime imager (Gardner-Watkins et al. 2023).

We used `AstroImageJ` to extract the data, and added the expected scintillation noise errors following Stefansson et al. (2017). After testing a number of aperture settings and reference stars, we found that an aperture radius of 25 pix, inner sky background annulus of 100 pix, and outer annulus of 150 pix yielded the highest-precision extraction. We adopt this extraction for our analysis.

[37] https://archive.lco.global/

2.5.3. RBO 0.6 m Photometry

On the night of 2023 April 23, we observed a full TOI-2015 b transit using the Apogee Alta F16 camera on the 0.6 m telescope at Red Buttes Observatory (RBO; Kasper et al. 2016) in Wyoming. We used the Bessell *I* filter and 240 s exposures. In the 2×2 binning mode, the detector has a gain of $1.4\,e^{-}\,ADU^{-1}$ and a read noise of $16\,e^{-}$. The plate scale is $0\farcs72\,pix^{-1}$, with a $25' \times 25'$ field of view.

We extracted the photometry using a custom `python` pipeline adapted from the one outlined in Monson et al. (2017). After testing a number of reference star and aperture combinations, we chose to use a 6 pix aperture with an inner sky radius of 20 pix and outer sky radius of 40 pix.

2.5.4. ARC 3.5 m Photometry

We obtained a full transit of TOI-2015 b on the night of 2023 April 23 with the Astrophysical Research Consortium Telescope Imaging Camera (ARCTIC; Huehnerhoff et al. 2016) on the Astrophysical Research Council (ARC) 3.5 m telescope at the Apache Point Observatory. Due to weather, we chose to observe with slight defocusing in the narrowband Semrock filter (8570/300 Å; Stefansson et al. 2017, 2018b), which avoids atmospheric absorption lines, using 40 s exposures. The data were reduced using `AstroImageJ`. After experimenting with a number of apertures and reference stars, we chose to use a 16 pix aperture with a 25 pix inner sky background annulus and 35 pix outer annulus.

On the night of 2023 May 3, we observed another full transit of TOI-2015 b. We used the SDSS i' filter and 45 s exposures with the Engineered Diffuser available on ARCTIC (Stefansson et al. 2017). We used the `astroscrappy` code to correct for cosmic-ray hits and reduced the photometry with `AstroImageJ` using an aperture of 12 pix and inner and outer sky annulus of 20 and 40 pix, respectively, for our final reduction.[38]

During both nights, we used 4×4 binning with a gain of $1.9\,e^{-}\,ADU^{-1}$ and a read noise of $6.6\,e^{-}$. We also used the quad amplifier with the 2.7 s fast readout rate mode. In this binning mode, ARCTIC has a plate scale of $0\farcs456\,pix^{-1}$, and a $7\farcm9 \times 7\farcm9$ field of view.

3. Stellar Parameters

3.1. Spectroscopic Parameters

To obtain spectroscopic constraints on the effective temperature ($T_{\rm eff}$), metallicity ([Fe/H]), surface gravity ($\log g$), and projected rotational velocity ($v \sin i_\star$) of TOI-2015, we used the `HPF-SpecMatch` code (Stefansson et al. 2020a).[39] This code uses a two-step chi-squared minimization process to compare a target spectrum to an as-observed spectral library of 166 well-characterized stars ($2700\,K < T_{\rm eff} < 5990\,K$). The final target parameters are determined with a weighted average of the five best-fitting library star parameters.

Using `HPF-SpecMatch`, we determine the following stellar parameters for TOI-2015: $T_{\rm eff} = 3194 \pm 56$ K, $\log g = 4.95 \pm 0.04$, and $[Fe/H] = 0.05 \pm 0.14$, where the uncertainties are calculated using a leave-one-out cross-validation process on the full spectral library. For the projected rotational velocity, we obtain $v \sin i_\star = 3.2 \pm 0.6\,km\,s^{-1}$, where the

[38] https://github.com/astropy/astroscrappy
[39] https://github.com/gummiks/hpfspecmatch

Table 1
Summary of TOI-2015 Stellar Parameters Used in This Work

Parameter	Description	Value	References
Equatorial Coordinates, Proper Motion, and Spectral Type:			
α_{J2000}	R.A., J2015.5	15:28:31.84	Gaia DR3
δ_{J2000}	decl., J2015.5	+27:21:39.86	Gaia DR3
μ_α	Proper motion (R.A.; mas yr^{-1})	-56.244 ± 0.010	Gaia DR3
μ_δ	Proper motion (decl.; mas yr^{-1})	63.807 ± 0.014	Gaia DR3
Equatorial Coordinates, Proper Motion, and Spectral Type:			
B	APASS Johnson B mag	17.134 ± 0.102	APASS
V	APASS Johnson V mag	16.11 ± 0.2	APASS
g'	APASS Sloan g' mag	16.284 ± 0.018	APASS
r'	APASS Sloan r' mag	14.988 ± 0.019	APASS
i'	APASS Sloan i' mag	13.358 ± 0.017	APASS
TESS-mag	TESS magnitude	12.8387 ± 0.007	TIC
J	2MASS J mag	11.118 ± 0.022	2MASS
H	2MASS H mag	10.519 ± 0.019	2MASS
K_S	2MASS K_S mag	10.263 ± 0.019	2MASS
WISE1	WISE1 mag	10.098 ± 0.022	WISE
WISE2	WISE2 mag	9.926 ± 0.02	WISE
WISE3	WISE3 mag	9.771 ± 0.039	WISE
WISE4	WISE4 mag	9.319	WISE
Spectroscopic Parameters from `HPF-SpecMatch`:			
$T_{\rm eff}$	Effective temperature in K	3194 ± 56	This work
[Fe/H]	Metallicity in dex	0.05 ± 0.14	This work
log(g)	Surface gravity in cgs units	4.95 ± 0.04	This work
Model-dependent Stellar SED and Isochrone fit Parameters[a]:			
Spectral Type	⋯	M4	This Work
M_*	Mass in $M_\odot$	$0.342^{+0.021}_{-0.025}$	This work
R_*	Radius in $R_\odot$	0.333 ± 0.011	This work
ρ_*	Density in g cm^{-3}	$12.98^{+1.1}_{-0.97}$	This work
Age	Age in Gyr from SED fit	$6.8^{+4.7}_{-4.6}$	This work
L_*	Luminosity in $L_\odot$	$0.01050^{+0.00044}_{-0.00052}$	This work
d	Distance in pc	$47.32^{+0.04}_{-0.03}$	Gaia DR3, Bailer-Jones
π	Parallax in mas	21.131 ± 0.018	Gaia DR3
Other Stellar Parameters:			
$v \sin i_\star$	Stellar rotational velocity in km s^{-1}	3.2 ± 0.6	This work
$P_{\rm rot}$	Rotation period in days	8.7 ± 0.9	This work
Age	Gyrochronological age in Gyr[b]	1.1 ± 0.1	This work
$i_\star$	Stellar inclination in degrees	$90° \pm 20°$	This work
RV	Absolute radial velocity in km s^{-1} (γ)	-32.04 ± 0.17	This work
U	Galactic U velocity (km s^{-1})	-30.60 ± 0.07	This work
V	Galactic V velocity (km s^{-1})	-11.51 ± 0.07	This work
W	Galactic W velocity (km s^{-1})	-17.95 ± 0.14	This work

Notes. References: TIC (Stassun et al. 2018, 2019), Gaia DR3 (Gaia Collaboration et al. 2023), APASS (Henden et al. 2015), 2MASS/WISE (Cutri et al. 2021), Bailer-Jones (Bailer-Jones et al. 2021).
[a] `EXOFASTv2`-derived values using MIST isochrones with the Gaia parallax and spectroscopic parameters from *a* as priors.
[b] Using the gyrochronological age relation for M4–M6.5 dwarfs in Engle & Guinan (2023). Uncertainties are likely underestimated.

uncertainty adopted is the standard deviation of the $v \sin i_\star$ values from running our spectral matching analysis on the seven orders cleanest of tellurics (8540–8640, 8670—8750, 8790–8885, 9940–10055, 10105–10220, 10280–10395, and 10460–10570 Å). Overall, the two best-fitting stars are GJ 1289 and GJ 4065, which have spectral types of M4.5 (Lépine et al. 2013), and M4 (Newton et al. 2014), respectively. As both are in general agreement, we adopt a spectral type of M4 for TOI-2015.

3.2. Spectral Energy Distribution

We fit the spectral energy distribution (SED) of TOI-2015 using the exoplanet and stellar fitting software package `EXOFASTv2` (Eastman et al. 2019). This allows us to constrain values such as mass, radius, and age for TOI-2015. The SED fit requires three primary inputs: available literature photometry data, parallax given by Gaia (Bailer-Jones et al. 2021), and the spectroscopic parameters derived using `HPF-SpecMatch`. As the model-dependent SED parameters for $T_{\rm eff}$, log g, and [Fe/H] agree with the spectroscopic parameters we obtain with `HPF-SpecMatch`, we do not list them in Table 1 for simplicity.

3.3. TOI-2015 is a Fully Convective Star

We also place TOI-2015 in the context of the transition between partially and fully convective M-dwarf host stars (Limber 1958; Kumar 1963), by utilizing the eponymous "Jao Gap" to distinguish between the two regions in a color–magnitude diagram (CMD; Baraffe & Chabrier 2018; Jao et al. 2018; Feiden et al. 2021). We obtain a sample of stars with parallax greater than 20 mas (i.e., closer than 50 pc) queried from Gaia Data Release 3 (DR3; Gaia Collaboration et al. 2023) and subsequently cross-match with the Two Micron All Sky Survey (2MASS; Cutri et al. 2003). Finally, we also apply a luminosity cut to exclude red giants based on absolute K_s magnitudes from Cifuentes et al. (2020) as $4.7 < M_{K_s} < 10.1$. Figure 4 shows the resulting CMD, which shows that TOI-2015 is below the transition feature in the CMD and hence a fully convective M dwarf.

3.4. Stellar Rotation and Age

The TESS data show clear periodic out-of-transit rotational modulations. As further discussed in Section 4.2, we model the out-of-transit variability using a quasiperiodic Gaussian process (GP) kernel following Stefansson et al. (2020b). This yields a best-fit GP periodicity of $P_{\rm rot,TESS} = 6.2^{+1.0}_{-0.7}$ days.

To gain further insight into the stellar rotation period, we also examined the available ground-based photometry from the Zwicky Transient Facility (ZTF; Masci et al. 2019). Figure 5 shows the photometry in the z_g, z_r, and z_i filters, along with Lomb–Scargle periodograms of the respective filters. From these plots, we see that all filters show a peak at $P_{\rm rot,ZTF} = 8.7$ days. For both the z_g and the z_r filters, the peak has a false-alarm probability (FAP) less than 1%, whereas z_i has a higher FAP. We attribute the higher-z_i FAP to the shorter time baseline and fewer data points available for the filter. Figure 5 also shows periodograms as calculated using the TESS systematics-insensitive periodogram package (TESS-SIP; Hedges et al. 2020) for both available TESS sectors. Although we examine Sectors 24 and 51 separately in this analysis, TESS-SIP is capable of creating periodograms while simultaneously accounting for TESS systematics within and across sectors. To build a periodogram, TESS-SIP simultaneously fits systematic regressors and sinusoidal components to the time-series data, including regularization terms to avoid overfitting. From Figure 5, we see that TESS Sector 24 shows a peak consistent with 8.7 days, whereas TESS Sector 51 shows a

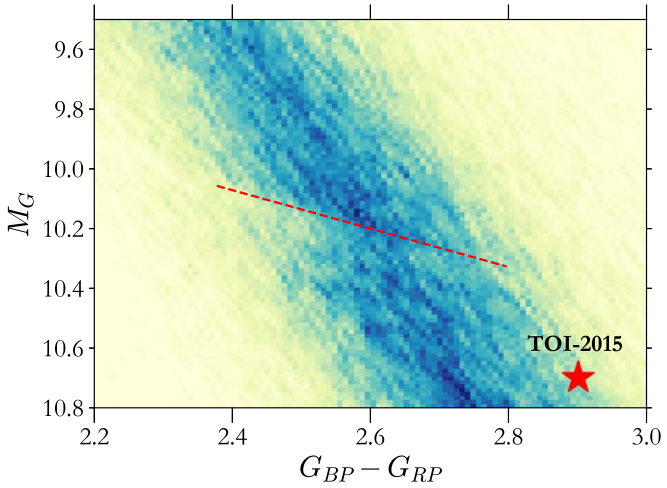

Figure 4. Kernel density estimate for a CMD based on Gaia DR3 showing M dwarfs closer than 50 pc. The dashed line shows the upper edge of the Jao Gap (Jao et al. 2018), which is the transition zone between partially and fully convective M dwarfs. TOI-2015 (red star) is below this transition zone, suggesting that it is a fully convective M dwarf.

peak at 6.3 days. While running additional tests on Sector 51, we saw that the periodogram for this sector is sensitive to the maximum period chosen. We attribute this sensitivity to the lack of data available in Sector 51 due to large gaps in the TESS photometry.

Given that the ZTF data consistently show peaks at 8.7 days in all three filters over many years, which TESS Sector 24 agrees with, we adopt a final stellar rotation period of $P_{\rm rot} = 8.7 \pm 0.9$ days, where we have conservatively adopted a 10% uncertainty on the rotation period.

With detections of both the photometric rotation period and the rotational velocity, we can estimate the stellar inclination. To estimate accurate posteriors for the stellar inclination $i_\star$, we use the formalism of Masuda & Winn (2020), which accurately accounts for the correlated dependence between $v \sin i_\star$ and the equatorial velocity $v_{\rm eq}$ as calculated from $R_\star$ and $P_{\rm rot}$. As the $v \sin i_\star$ measurement does not distinguish solutions between $i_\star$ and $180^\circ - i_\star$, we calculate two independent solutions between 0°–90° and 90°–180°. Using our values for $P_{\rm rot}$, $v \sin i_\star$, and $R_\star$, we obtain two mirrored posteriors around the highest-likelihood inclination of 90°, which together yield an inclination constraint of $i_\star = 90^\circ \pm 20^\circ$. Alternatively, taking a look at only the 0°–90° solution, our posterior constraint on the stellar inclination is $i_\star > 80^\circ$ at 68% confidence.

Reliable age determinations for M stars is difficult due to the slow evolution of their fundamental properties (e.g., Laughlin et al. 1997), and the apparent rapid transition from fast to slow rotation states (Newton et al. 2017). West et al. (2015) noted that all M1V–M4V stars in their MEarth sample rotating faster than 26 days are magnetically active. Using the gyrochronological relationship in Engle & Guinan (2023) calibrated for M4–M6.5 stars, we infer an age of 1.1 ± 0.1 Gyr. This age estimate is in line with expectations of a younger and active star, agreeing with the Ca II infrared triplet (Ca II IRT) emission seen in the HPF spectra, the flares seen in TESS, and the moderate $v \sin i = 3.2 \pm 0.6$ km s^{-1} value, although the age uncertainties are likely underestimated.

We note that the SED fit we ran for TOI-2015 provides an age estimate, as well, with a broad constraint of $6.8^{+4.7}_{-4.6}$ Gyr. For this study, we adopt the rotation-based age of 1.1 ± 0.1 Gyr as the primary age estimate for the system.

Additionally, we calculated the galactic space velocities U, V, and W of TOI-2015 (see Table 1) using the `GALPY` package (Bovy 2015). Following Carrillo et al. (2020), we calculate membership probabilities of 99%, 1%, and $\ll$1% for TOI-2015 as a member of the galactic thin-disk, thick-disk, and halo populations, respectively. Further, from the galactic velocities, we used the BANYAN Σ tool (Gagné et al. 2018) to see if TOI-2015 is a member of any known young stellar associations, from which we rule out membership to 27 well-characterized young associations within 150 pc with 99.9% confidence.

3.5. Spectroscopic Stellar Activity Indicators

Magnetic activity can create planet-like signals in RV data (e.g., Robertson et al. 2014). To probe corresponding periodicities in the HPF activity indicators, Figure 6 compares generalized Lomb–Scargle periodograms of the HPF RVs along with the HPF differential line width (dLW) indicator, chromatic index (CRX), and the Ca II NIR triplet indicators (Ca II IRT).[40] To generate the periodograms, we used the `astropy.timeseries` package, which we also used to calculate associated FAPs using the `bootstrap` method available in the package. The TOI-2015 periodograms show small hints of a peak at the known planet period, but it is not considered significant, with FAP > 1%.

From visual inspection of the HPF spectra, we see clear evidence of chromospheric emission in the cores of the Ca II IRT lines, confirming that TOI-2015 is an active star. However, this chromospheric variability does not show an apparent corresponding periodicity with either the known planet period or the stellar rotation period, as seen in Figure 6. The lack of significant peaks in either the RV or dLW periodograms at $P_{\rm rot} = 8.7$ days suggests that the RV impact of stellar activity is not a dominant signal for this star given our median RV precision level of $\sim$15 m s^{-1}. Additionally, we show the window function of the RVs in Figure 6, which reveals a peak at the lunar cycle of $P \sim 28$ days, as the HPF observations were preferentially executed during bright time in the HET queue. Table 6 in Appendix B lists the values of the RVs and the activity indicators used in this work.

4. Transit, Radial Velocity, and Transit Timing Variation Modeling

4.1. Search for Additional Transiting Planets in TESS

To identify potential additional transiting planets, we used the `transitleastsquares` (`TLS`; Hippke & Heller 2019) code to look for periodic transit-like features in the TESS photometry.[41] We extracted the PDCSAP 2 minutes cadence data using the `lightkurve` package (Lightkurve Collaboration et al. 2018). Using `TLS`, we removed outliers and detrended the photometry with a Savitzky–Golay high-pass filter of window length 501 cadences. We chose this ∼17 hr window to help remove out-of-transit variability, while having a minimal impact on the transit features. Due to the 2 yr gap between Sectors 24 and 51, we chose to analyze each sector individually.

[40] The wavelength region definitions for our Ca II IRT activity index are listed in Stefansson et al. (2020b).
[41] https://transitleastsquares.readthedocs.io/en/latest/index.html

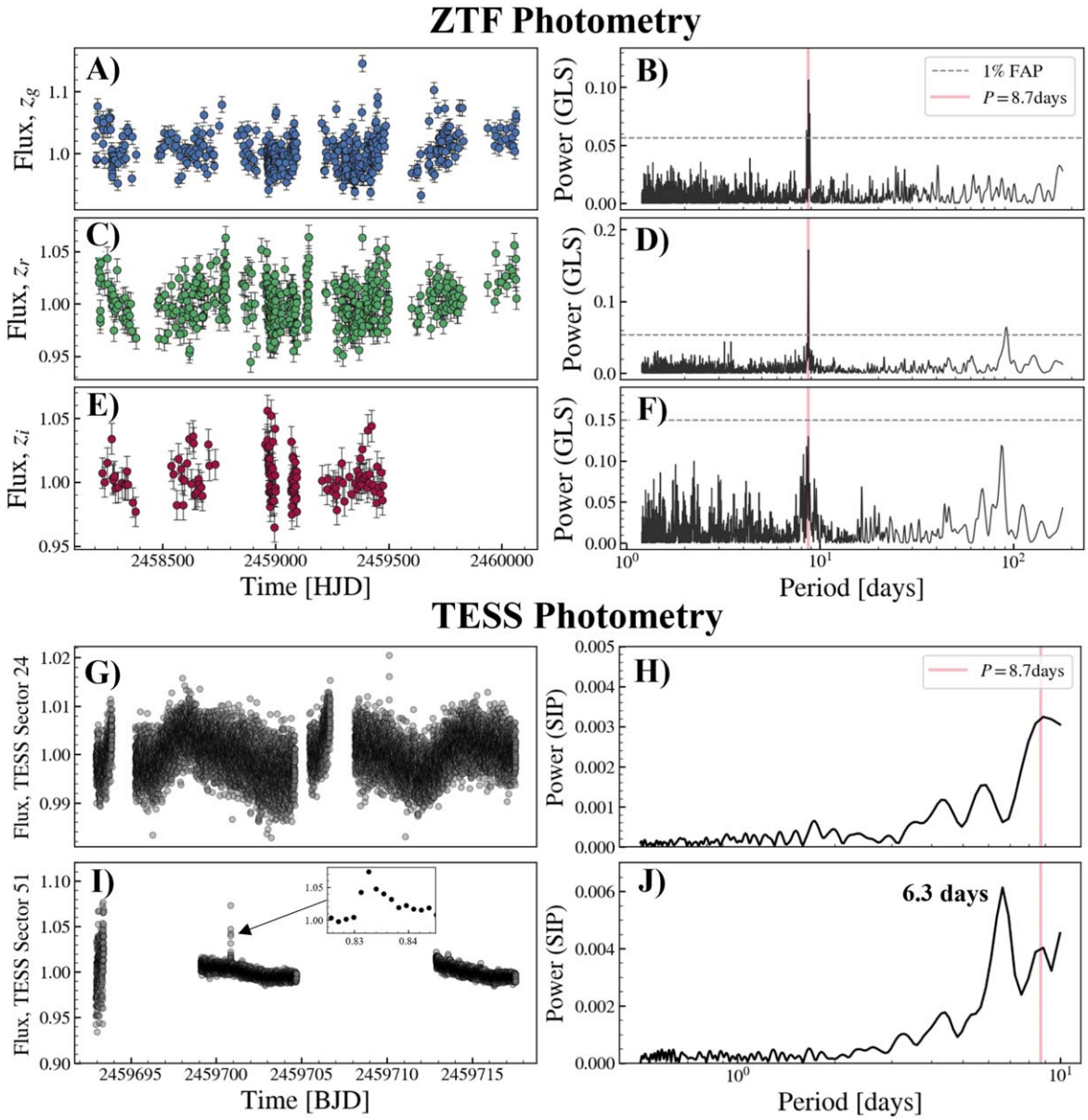

Figure 5. Out-of-transit photometry from ZTF and TESS. (A)–(F) ZTF photometry and associated generalized Lomb–Scargle periodograms in the z_g, z_r, and z_i filters. All filters show a peak at 8.7 days (red vertical line). (G)–(J) TESS photometry and associated TESS-SIP plots for Sectors 24 and 51. TESS Sector 24 shows a peak consistent with 8.7 days, whereas Sector 51 shows a peak at 6.3 days. We attribute the latter to low data coverage and large gaps in the TESS data. We adopt a rotation period of 8.7 ± 0.9 days. In panel (I), we also show a zoomed-in view of one of the flares in the TESS photometry.

Figure 7 shows the `TLS` power spectra for TESS Sectors 24 and 51 before and after masking out the TOI-2015 b transits. Using `TLS`, we find the 3.3490 days period of planet b is featured strongly in the resulting power spectra (above the 0.1% FAP line). To identify other potential transiting companions, we masked out all TOI-2015 b in-transit regions in the TESS light curve, with windows 3 times wider than the transit duration to account for TTVs. After searching the masked data, the TLS power spectrum revealed no significant peaks (FAP $< 0.1\%$, correlating to a `TLS` signal detection efficiency, SDE, >8.3, indicative of additional transiting planets).

From this analysis, we conclude there is evidence for only one transiting planet in the system, and that the orbiting companion causing the TTVs that we observe is not transiting in the available TESS data.

4.2. Joint Transit and RV Fit

As such, we jointly modeled the TESS and ground-based photometry and HPF RVs using the `juliet` software package (Espinoza 2018) assuming a single transiting planet. We utilize dynamic nested sampling with the `dynesty` sampler (Speagle 2020) to estimate the posterior parameter space of our joint fit. We parameterized the transits using the r_1 and r_2 parameters from Espinoza (2018), which probe only the full range of physically possible values for scaled radius R_p/R_* and impact parameter b. We also used stellar density ρ_* and the Kipping (2013) quadratic limb-darkening parameterizations q_1 and q_2 as parameters in the fit.

Because the TESS photometry showed evidence of periodic out-of-transit variability, we incorporate GPs in our model. To fit for the periodic out-of-transit variability, we applied the `celerite` (Foreman-Mackey et al. 2017) quasiperiodic

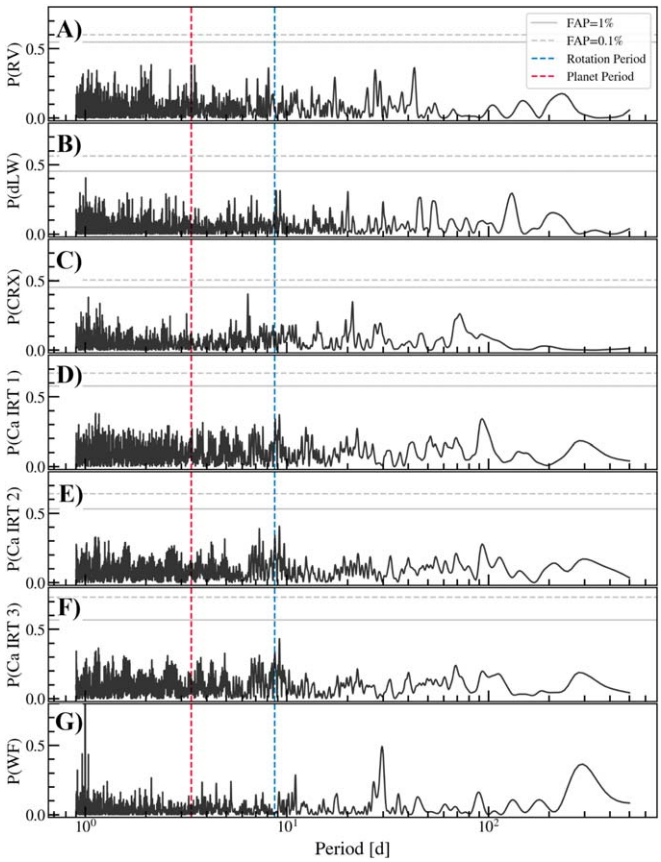

Figure 6. Generalized Lomb–Scargle periodograms of the HPF RVs and HPF activity indicators. (A) HPF RVs. (B) HPF differential line width (dLW) indicator. (C) Chromatic activity index (CRX). (D)–(F) Ca II infrared triplet (IRT) line indicators. (G) Window function (WF) of the observations. The known planet period and the stellar rotation period are denoted with the vertical blue and red dashed lines, respectively. False-alarm probabilities (FAPs) of 1% and 0.1% calculated using a bootstrap method are denoted with the gray solid and gray dashed lines, respectively. Although we see a hint of a peak near the known planet period, it is not significant (FAP $> 1\%$). For the activity indicators, we see no significant peaks at the known planet or stellar rotation periods. Periodograms (A)–(F) are normalized using the formalism in Zechmeister & Kürster (2009), while the WF in panel (G) is normalized such that the highest peak has a power of 1.

kernel to the TESS photometry. GPs were not needed for ground-based data, because these few-hour observations are not long enough for a significant rotational modulation signal to be detected. The quasiperiodic kernel in `celerite` is parameterized by the following hyperparameters: a GP amplitude B, an additive factor impacting the amplitude C, the length scale of the exponential part of the GP L, and the GP period $P_{\rm GP}$. To account for TTVs, we used `juliet`'s TTV modeling feature. We used a uniform prior with a 0.2 day window around the expected transit midpoint for each of the 17 transits from the TESS and ground-based data.

Figures 8 and 9 summarize the results from the fit, showing the best-fit joint model for the photometry and RVs, respectively. Additionally, Figure 14 in Appendix A1 shows the individual TESS transits along with the best-fit transit models accounting for the TTVs. The priors and final parameters are summarized in Table 2, and Table 4 in Appendix A2 shows the individually derived TTV midpoints for each transit. Those TTV midpoints are further fit and discussed in Section 4.3 to constrain the possible parameters of the second planet candidate.

The fit above assumed a circular orbit for planet b. In addition to the circular fit, we experimented with running a fit where we let the eccentricity vary. In doing so, we obtain a best-fit eccentricity of $e = 0.23 \pm 0.07$ with a log-evidence value of $\ln(Z) = 88489.91$. Whereas the circular fit has a log-evidence value of $\ln(Z) = 88488.80$. As this log-evidence value is only $\Delta \ln(Z) = 1.1$ or $\Delta Z = 3.0$ larger, we consider the models to be statistically indistinguishable. Here we have followed the suggestion in Espinoza et al. (2019) of requiring at least $\Delta \ln(Z) = 2$ or equivalently $\Delta Z = 7.4$ as a threshold for statistical significance. As such, we elect to adopt the posteriors from the simpler circular fit, as listed in Table 2.

4.3. Joint TTV and RV Fit

Next, we searched for two-planet solutions consistent with the TTVs and RVs of TOI-2015 b. Large sinusoidal TTVs are typical in systems near mean-motion resonances, and so here we focus on solutions for which the period ratio of the second planet candidate and TOI-2015 b is around 2:1, 3:2, and 4:3. Throughout this section, the TTVs are computed with full N-body integrations, assuming coplanar orbits and ignoring any relativistic corrections. Because the 2 minutes cadence TESS photometry shows no evidence of a second transiting planet (including at the given period ratios; see Section 4.1), it is unclear whether the assumption of coplanarity is correct. However, the lack of transit provides little information in this aspect; given TOI-2015 b's impact parameter of ≈ 0.7, an outer planet candidate with a period ratio $\gtrsim 1.7$ does not transit even assuming perfect coplanarity. It is not our goal here (nor is it practical) to explore all possible period ratios and mutual orbital inclinations for the second planet candidate. Rather, we would like to know whether reasonable two-planet solutions exist—and if so, what some of them look like—to guide future observations to better characterize this system, as well as to check the robustness of the RV mass that was derived ignoring the second planet candidate.

First, we combined `TTVFast` (Deck et al. 2014) and `MultiNest` (Feroz et al. 2009; Buchner et al. 2014), as described in Masuda (2017), to find optimal solutions around 2:1, 3:2, and 4:3 resonances, setting narrow priors on the period of the outer planet candidate. The prior ranges were chosen so that the expected super-period (Lithwick et al. 2012) matches the $\sim$430 days periodicity seen in the data. We obtained the maximum-likelihood parameters from the `MultiNest` runs, and performed chi-squared optimization starting from the solution, using the trust region reflective method implemented in `scipy.optimize.curve_fit`. In all cases, we found acceptable solutions that provide $\chi^2 \approx 10$ for 17 data points and 10 free parameters (i.e., $\chi^2/\mathrm{dof} = 10/7 \approx 1.4$).

We then perform a joint TTV-RV fit for each of the three period ratios. Here we obtain samples from the joint posterior distribution for the system parameters θ conditioned on the TTV data $t^{\rm obs}$ and RV data $v^{\rm obs}$:

$$p(\theta | t^{\rm obs}, v^{\rm obs}) \propto \mathcal{L}(\theta)\, \pi(\theta). \quad (1)$$

Here π denotes the prior probability distribution for θ that is assumed to be separable for each parameter (see Table 3). We

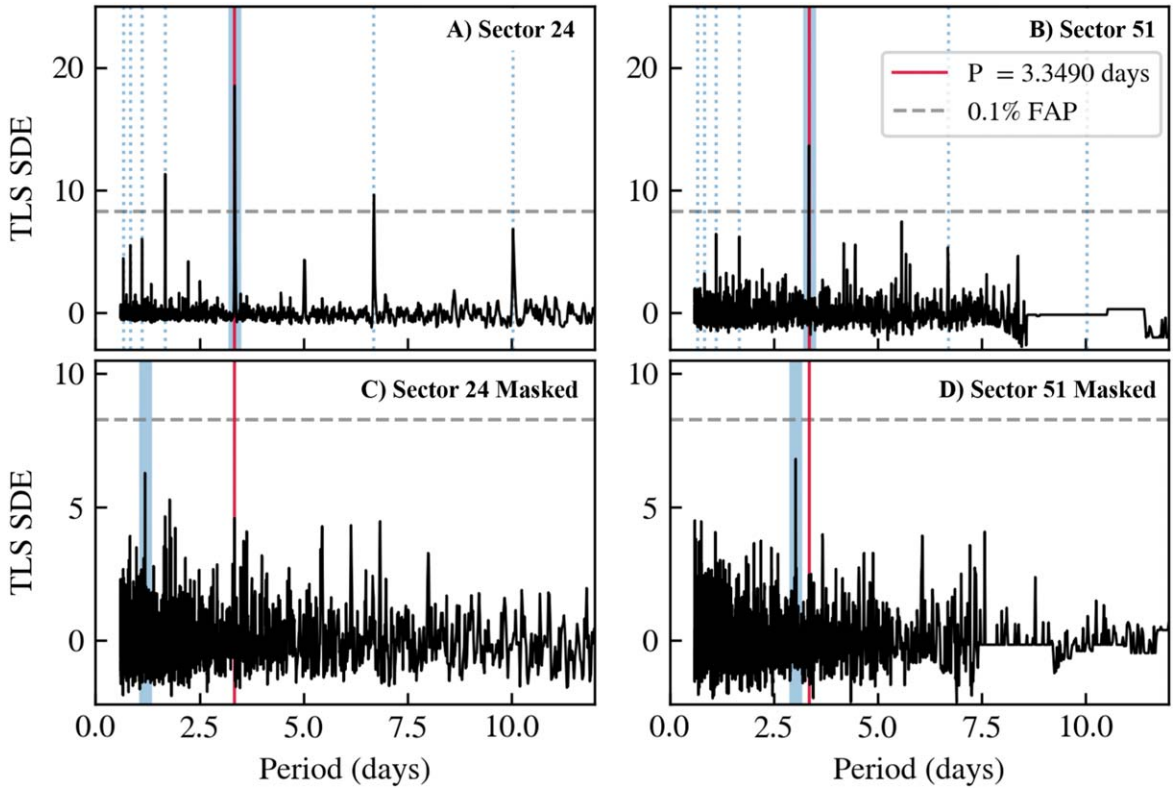

Figure 7. Transit least-squares signal detection efficiency (TLS SDE) power spectra as a function of orbital period for TESS Sectors 24 and 51. The solid blue bands indicate the maximum peak of each power spectrum. The blue dotted lines in panels (A) and (B) are the integer harmonics of the 3.3490 days orbital period of TOI-2015 b in red. The gray dashed lines represent 0.1% false-alarm probability (FAP). We do not detect signals of an additional transiting companion in the TESS data.

adopt the following log-likelihood function:

$$\ln \mathcal{L}(\theta) = -\frac{1}{2}\sum_i \left(\frac{t_i^{\rm obs} - t_i^{\rm model}}{\sigma_i^{\rm obs}} \right)^2 - \frac{1}{2}\sum_{i,j} (v_i^{\rm obs} - v_i^{\rm model})(K^{-1})_{ij}(v_j^{\rm obs} - v_j^{\rm model}) - \frac{1}{2}\ln\det K + \text{constant}, \quad (2)$$

where $t^{\rm model}$ is the modeled transit midpoint including the TTV and $v^{\rm model}$ is the expected RV, both computed via full N-body integration. The N-body code is implemented in `JAX` (Bradbury et al. 2018) to enable automatic differentiation with respect to the input orbital elements and mass ratios (see also Agol et al. 2021), and is available through GitHub as a part of the `jnkepler` package (K. Masuda 2024, in preparation).[42] In our model, we assume that the TTV errors follow independent zero-mean Gaussian distributions whose widths are the assigned timing errors as listed in Table 4. In evaluating the likelihood for the RV data, we use a GP to model a correlated noise component that may exist given the activity of the star. Here we adopt a simple harmonic oscillator covariance function K that corresponds to the following power spectral density:

$$S(\omega) = \sqrt{\frac{2}{\pi}} \frac{S_0\,\omega_0^4}{(\omega^2 - {\omega_0}^2)^2 + {\omega_0}^2\,\omega^2/Q^2},$$

which was parameterized by the undamped period of the oscillator $\rho = 2\,\pi/\omega_0$, the standard deviation of the process $\sigma = \sqrt{S_0\,\omega_0\,Q}$, and the quality factor Q (Foreman-Mackey et al. 2017). We also included a jitter term whose square was added to the diagonal elements of the covariance matrix. The GP log-likelihood was evaluated using the `JAX` interface of `celerite2` (Foreman-Mackey et al. 2017; Foreman-Mackey 2018). Leveraging the differentiable $\mathcal{L}(\theta)$, we sample from $p(\theta|t^{\rm obs}, v^{\rm obs})$ using Hamiltonian Monte Carlo and the No-U-Turn Sampler (Duane et al. 1987; Betancourt 2017) as implemented in `NumPyro` (Bingham et al. 2019; Phan et al. 2019). We run six chains in parallel, setting the target acceptance probability to be 0.95 and the maximum tree depth to be 11.

After obtaining posterior samples, we performed longer-term integration for a subset of the samples to remove solutions that quickly become unstable. We use the `mercurius` integrator (Rein et al. 2019) in the `REBOUND` package (Rein & Liu 2012) to integrate 10^8 inner orbits (i.e., $\sim$1 Myr). We flagged a solution to be unstable if the semimajor axis of TOI-2015 b changed by more than 1% during the integration, in which case the period ratio of the two planets changed by more than $\sim$10%, making the current near-resonant architecture implausible (Dai et al. 2023).

The results of the joint TTV-RV modeling are summarized in Table 3. For the 2:1 solution, the effective number of samples reached 50 and the split Gelman–Rubin statistic achieved $\hat{R} < 1.1$ (Gelman et al. 2014, Chapter 11) after running 20,000 steps for most parameters except for the transit midpoint (τ_c) and period (P_c) of the second planet candidate.

[42] https://github.com/kemasuda/jnkepler

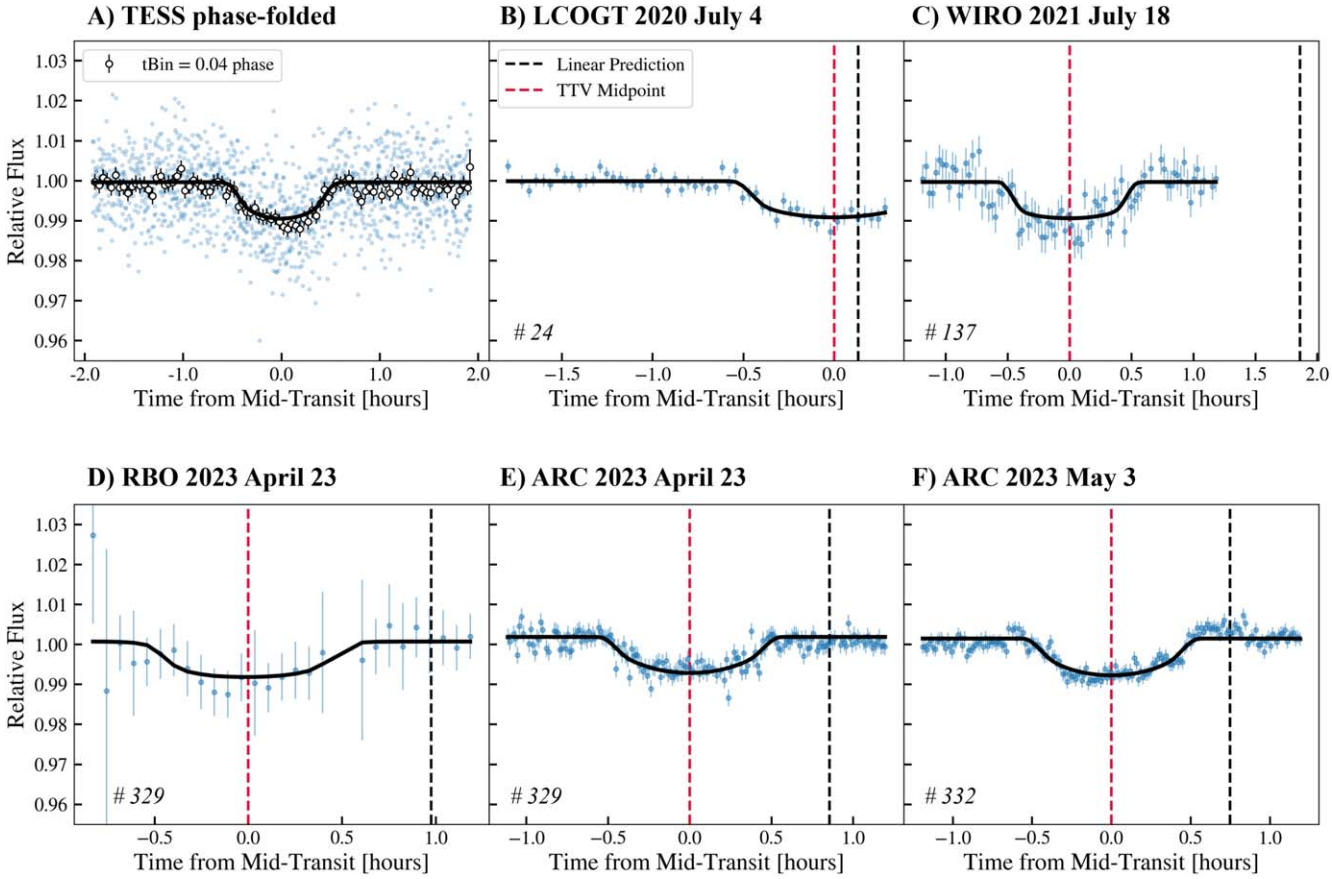

Figure 8. TOI-2015 phased photometry from `juliet` joint TTV fit. Data points are plotted in blue. The best-fit transit models are plotted with solid black lines. The vertical black lines represent the expected linear midpoint predictions, and the vertical red lines are the true TTV midpoints. The transit number (first TESS transit is #0) is labeled in the bottom-left corner of each ground-based transit. (A) Phase-folded photometry of 12 TESS transits. White points are $N_{\rm Bin} = 15$ binned data. (B) LCOGT partial-transit photometry. (C) WIRO full-transit photometry. (D) RBO full-transit photometry. (E) ARC 2023 April full-transit photometry. (F) ARC 2023 May full-transit photometry.

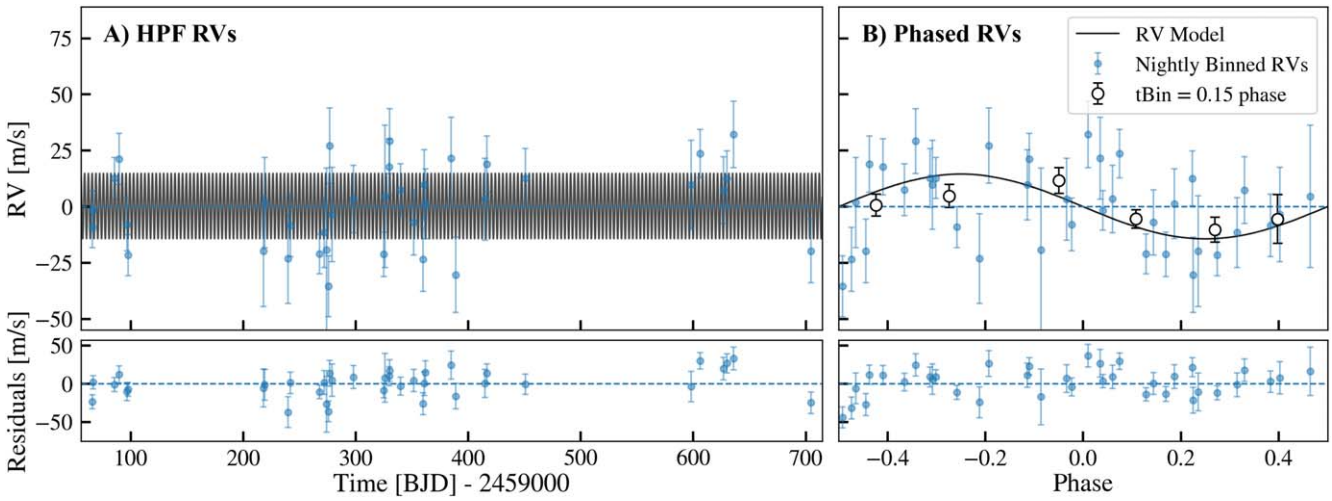

Figure 9. HPF RV measurements. RVs (blue points) are plotted with respect to the baseline (horizontal dashed line) and the best-fit model (bold black line). (A) RVs as a function of time. (B) RVs phase-folded at the period of TOI-2015 b. Residuals are displayed in the corresponding lower panels. The RV data are listed in Table 6 in Appendix B. TOI-2015 b is evident in the RVs, but there are no additional planetary signals.

The poorer convergence for these two parameters is due to strong and complicated degeneracy between these parameters and eccentricity vectors (see Figure 15), and their summary statistics may be of limited accuracy. We tested stability for 10,000 randomly chosen posterior samples and found that >90% survived. Thus the 2:1 solution qualifies as a valid explanation for the TTV and RV data. From the joint TTV-RV fit, we inferred the masses of $m_b = 13.3^{+4.7}_{-4.5}\ M_\oplus$ for TOI-2015 b and $m_c = 6.8^{+3.5}_{-2.3}\ M_\oplus$ for the outer planet candidate. This mass for TOI-2015 b is consistent with the value from our `juliet`

Table 2
Median Values and 68% Credible Intervals from `juliet` Joint Photometry and RV Fit

Parameter	Description	Prior	TOI-2015 b
Orbital Parameters:			
$P_{\rm orb}$	Orbital period (days)	$\mathcal{U}(3.33, 3.36)$	$3.348968^{+0.000004}_{-0.000004}$
T_C	Transit midpoint–2458000 ($\rm BJD_{TDB}$)	$\mathcal{U}(955.9, 956.1)$	$956.0226^{+0.0009}_{-0.0009}$
r_1	Espinoza (2018) parameterization for impact parameter b	$\mathcal{U}(0, 1)$	$0.797^{+0.020}_{-0.022}$
r_2	Espinoza (2018) parameterization for scaled radius R_p/R_*	$\mathcal{U}(0, 1)$	$0.0933^{+0.0020}_{-0.0020}$
R_p/R_*	Scaled radius	⋯	$0.0933^{+0.0020}_{-0.0020}$
a/R_*	Scaled semimajor axis	⋯	$19.46^{+0.47}_{-0.51}$
b	Impact parameter	⋯	$0.696^{+0.031}_{-0.033}$
e	Eccentricity	0	0
ω	Argument of periastron (deg)	90	90
K	RV semi-amplitude ($\rm m\ s^{-1}$)	$\mathcal{U}(0, 100)$	$14.4^{+3.5}_{-3.6}$
Instrumental Terms:			
q_1	Limb-darkening parameter	$\mathcal{U}(0, 1)$	$0.70^{+0.20}_{-0.23}$
q_2	Limb-darkening parameter	$\mathcal{U}(0, 1)$	$0.60^{+0.25}_{-0.29}$
$\sigma_{\rm phot}$	Photometric jitter (ppm)	$\mathcal{J}(1, 5000)$	$8.9^{+37.3}_{-6.8}$
$\mu_{\rm phot}$	Photometric baseline	$\mathcal{N}(0, 0.1)$	$0.0003^{+0.0011}_{-0.0011}$
$\sigma_{\rm HPF}$	HPF RV jitter ($\rm m\ s^{-1}$)	$\mathcal{J}(0.1, 100)$	$4.75^{+4.86}_{-4.16}$
γ	HPF RV offset ($\rm m\ s^{-1}$)	$\mathcal{U}(-60, 60)$	$-2.2^{+2.3}_{-2.3}$
TESS Quasiperiodic GP Parameters:			
B	GP amplitude ($\rm ppm^2$)	$\mathcal{J}(10^{-6}, 1)$	$1.7\mathrm{e}-5^{+0.000006}_{-0.000004}$
C	GP additive factor	$\mathcal{J}(10^{-3}, 10^3)$	$0.028^{+0.25}_{-0.025}$
L	GP length scale (days)	$\mathcal{J}(10^{-2}, 10^5)$	$3.5^{+1.5}_{-1.0}$
Additional Derived Parameters:			
$R_{p,\oplus}$	Planet radius ($R_\oplus$)	⋯	$3.39^{+0.14}_{-0.13}$
$R_{p,\rm J}$	Planet radius ($R_{\rm J}$)	⋯	$0.302^{+0.012}_{-0.012}$
$\delta_{p,\rm K2}$	Transit depth	⋯	$0.0087^{+0.00038}_{-0.00037}$
a	Semimajor axis[a] (au)	⋯	$0.0301^{+0.0013}_{-0.0012}$
i	Transit inclination (deg)	⋯	$87.95^{+0.13}_{-0.14}$
$T_{\rm eq,0.0}$	Equilibrium temp. $a = 0.0$ (K)	⋯	$512.0^{+11.0}_{-11.0}$
$T_{\rm eq,0.3}$	Equilibrium temp. $a = 0.3$ (K)	⋯	$358.5^{+7.8}_{-7.7}$
S	Insolation flux ($S_\oplus$)	⋯	$11.47^{+1.0}_{-0.95}$
T_{14}	Transit duration	⋯	$0.0463^{+0.0010}_{-0.0010}$ (days)
T_{23}	Transit duration (days)	⋯	$0.0318^{+0.0018}_{-0.0018}$
τ	Ingress/egress duration (days)	⋯	$0.00719^{+0.00065}_{-0.00056}$
m_p	Planet mass ($M_\oplus$)	⋯	$16.4^{+4.1}_{-4.1}$
ρ_p	Planet density[b] ($\rm g\ cm^{-3}$)	⋯	$2.32^{+0.38}_{-0.37}$

Notes. TTV midpoints are displayed in Table 4 in Appendix A2. Prior denotations: $\mathcal{N}(\mu, \sigma)$ denotes a normal prior with mean μ and standard deviation σ; $\mathcal{U}(a, b)$ denotes a uniform prior with a start value a and end value b; and $\mathcal{J}(a, b)$ denotes a Jeffreys prior truncated between a start value a and end value b.
[a] Calculated from a/R_* and R_*.
[b] Calculated from m_p and r_p.

RV fitting assuming a single planet of $m_b = 16.4 \pm 4.1 M_\oplus$ from Table 2. The mass constraint from the joint TTV-RV fit is slightly less precise than the `juliet` value. This is not necessarily surprising given the additional degrees of freedom (i.e., eccentricity of TOI-2015 b, mass and orbital elements of the second planet candidate) introduced in the joint fit. The summary statistics in Table 3 are based on the samples that were classified to be stable. The TTV models corresponding to 20 of those samples are shown in Figure 10 with blue solid lines. The RV model corresponding to the maximum-likelihood sample is shown in Figure 11.

In contrast to the 2:1 solution, for the 3:2 and 4:3 solutions we could not obtain well-mixed chains. This appears to be due to strong multimodality in the ephemeris of the second planet candidate (τ_c and P_c). Thus we do not have well-defined estimates for the uncertainties of the parameters, and quote only medians of the posterior samples in Table 3 for these solutions. Interestingly, these solutions prefer larger mass ratios between planet b and candidate planet c than the 2:1 solution, and <50% out of the 200 randomly chosen posterior samples were found to be stable using the same criteria as adopted for the 2:1 solution.[43] As such, we deem these solutions less likely than the 2:1 case, although they are not fully excluded by the data. These solutions favor smaller masses for planet b than derived from the RV-only modeling, although the uncertainty is not well quantified.

In Figure 10, we show TTV models for 20 stable posterior samples from each solution extended to the future. While the three solutions converge around the existing data by construction, they diverge occasionally, especially around the local minima of the periodic TTV curves. Thus the three solutions

[43] We evaluated stability for smaller numbers of samples than we did for the 2:1 solution, because the purpose here is only to estimate the fraction of stable solutions.

Table 3
Median Values and 68% Credible Intervals from `jnkepler` Joint TTV and RV Fit

Parameter	Description	Prior	2:1 Solution	3:2 Solution	4:3 Solution
Parameters of Planet b:					
P_b	Orbital period (days)	$\mathcal{U}(3.149, 3.549)$	$3.3452^{+0.0004}_{-0.0004}$	3.3454	3.3448
$t_{0,b}$	Transit midpoint–2458000 (BJD_{TDB})	$\mathcal{U}(955.934, 956.134)$	$956.0342^{+0.0017}_{-0.0017}$	956.0326	956.0329
$e_b \cos \omega_b$	Eccentricity and argument of periastron	$e_b \sim \mathcal{N}_t(0, 0.1, 0)$	$0.077^{+0.083}_{-0.097}$	0.036	0.008
$e_b \sin \omega_b$	Eccentricity and argument of periastron	$\omega_b \sim \mathcal{U}_w(-\pi, \pi)$	$0.035^{+0.095}_{-0.126}$	0.027	0.001
M_b	Mass ($M_\oplus$)	$\mathcal{U}(0, 100)$	$13.3^{+4.7}_{-4.5}$	11.2	4.8
Parameters of Candidate Planet c:					
P_c	Orbital period (days)	$\mathcal{U}(\hat{P}_c - 0.2, \hat{P}_c + 0.2)$[a]	$6.7179^{+0.0107}_{-0.0073}$[b]	5.0524	4.4842
$\tau_{0,c} = (t_{0,c} - 2458955)/P_c$	Transit midpoint in units of P_c	$\mathcal{U}_w(0, 1)$	$0.33^{+0.15}_{-0.16}$[b]	0.21	0.09
$e_c \cos \omega_c$	Eccentricity and argument of periastron	$e_c \sim \mathcal{N}_t(0, 0.1, 0)$	$0.003^{+0.078}_{-0.065}$	0.05	0.03
$e_c \sin \omega_c$	Eccentricity and argument of periastron	$\omega_c \sim \mathcal{U}_w(-\pi, \pi)$	$-0.035^{+0.048}_{-0.049}$	0.00	−0.01
M_c	Mass ($M_\oplus$)	$\mathcal{U}(0, 100)$	$6.8^{+3.5}_{-2.3}$	2.4	1.3
Stellar Parameters:					
$M_\star$	Mass ($M_\odot$)	$\mathcal{N}_t(0.34, 0.025, 0.25)$	$0.340^{+0.025}_{-0.024}$	0.34	0.34
RV Model Parameters:					
ρ	Undamped period of the oscillator (days)	$\mathcal{N}_t(8.7, 0.87, 0.7)$	$8.7^{+0.9}_{-0.8}$	8.8	8.9
$\ln \tau$	Log of damping timescale of the process (days)	$\mathcal{U}(-3, 6)$	$0.9^{+3.6}_{-2.9}$	1.7	−0.83
$\ln \sigma$	Log of standard deviation of the process ($m\ s^{-1}$)	$\mathcal{U}(-3, 5)$	$1.1^{+1.2}_{-2.7}$	1.4	1.2
γ	HPF RV offset ($m\ s^{-1}$)	$\mathcal{U}(-30, 30)$	$2.3^{+3.1}_{-2.9}$	3.3	3.1
$\ln \sigma_{jit}$	Log of HPF RV jitter ($m\ s^{-1}$)	$\mathcal{U}(-1, 5)$	$1.7^{+0.7}_{-1.6}$	1.7	2.2

Notes. Orbital elements are the Jacobi elements defined at BJD–2458000 = 955. For the 3:2 and 4:3 solutions, only the median values are shown because Markov Chain Monte Carlo chains showed insufficient convergence. Prior denotations: $\mathcal{N}(\mu, \sigma)$ denotes a normal prior with mean μ, and standard deviation σ; $\mathcal{N}_t(\mu, \sigma, l)$ denotes $\mathcal{N}(\mu, \sigma)$ truncated at the lower bound l; $\mathcal{U}(a, b)$ denotes a uniform prior with a start value a and end value b; $\mathcal{U}_w(a, b)$ denotes a "wrapped" uniform prior where a and b are treated as the same points; and $\mathcal{J}(a, b)$ denotes a log-uniform prior truncated between a start value a and end value b.
[a] The values of $\hat{P}_c$ are $2P_b$, $(3/2)P_b$, and $(4/3)P_b$ for the 2:1, 3:2, and 4:3 solutions, respectively.
[b] Parameters showing poorer convergence.

may be more conclusively distinguished with future transit timing data of TOI-2015 b obtained at the right epoch. As such, we urge additional follow-up observations to help further constrain the potential period ratios in the system. The predicted transit times based on the 2:1 solution around this window are shown in Table 5. The transits could happen ∼100 minutes later than these values if the 3:2 or 4:3 solution is correct, or they could happen earlier, if the true solution lies in a part of the parameter space we did not explore.

5. Discussion

5.1. Mass and Bulk Composition

Figure 12 shows the mass and radius constraints of TOI-2015 b derived from our `juliet` joint photometry and RV fit. To gain an understanding of the possible composition of TOI-2015 b consistent with its observed mass and radius, the plot displays lines of constant density from the models of Zeng et al. (2019). TOI-2015 b's place among the density models suggests it is most likely volatile-rich.

To more precisely constrain the potential H/He mass fraction of TOI-2015 b, we use the composition model from Lopez & Fortney (2014). This is a two-component model consisting of a rocky core enveloped by a H/He atmosphere, where the atmosphere is the dominant driver of the planet radius. One parameter the model relies on is age. In this study, we calculated SED and rotational-based age estimates for TOI-2015. Interpolating the tables from Lopez & Fortney (2014) with the methodology in Stefansson et al. (2020b), we present mass fraction estimates for both age cases. When we assume the broad SED constraint of $6.8^{+4.7}_{-4.6}$ Gyr, we estimate a H/He mass fraction of 6.7%. Using the gyrochronological age estimate of 1.1 ± 0.1 Gyr, TOI-2015 b's mass and radius posteriors are compatible with a 6.0% H/He envelope. The planet's mass fraction is not largely sensitive to the difference in age. This supports the Lopez & Fortney (2014) models' demonstration of minimal contraction and change in the mass fraction for planets of age ∼1 Gyr and older due to rapid cooling occurring at very early ages (∼100 Myr). Just as we adopt the gyrochronological age to be the primary age estimate for TOI-2015 b, we too adopt a 6.0% H/He envelope as the mass fraction. Figure 12 shows the 50th percentile model that best fits the observed mass and radius of TOI-2015 b with the bold red line.

When we compare TOI-2015 b to other planets of similar mass and size, the well-studied M-dwarf planets GJ 436b and GJ 3470b are well-known targets with similar masses and radii to TOI-2015 b, both of which are known to have volatile-rich compositions and evaporating atmospheres (see, e.g., Bourrier et al. 2016 and Ninan et al. 2020, respectively). In Figure 12, we also compare TOI-2015 b to other M-dwarf planets that show evidence of TTVs (black points). Those systems include AU Mic (Plavchan et al. 2020) and K2-146 (Lam et al. 2020), where TOI-2015 b has a similar mass and radius to AU Mic b.

Constraining planet masses via RV observations for low-mass planets orbiting active stars can be challenging and observationally expensive, where TTVs provide a way to measure the mass independently of RVs. This is particularly advantageous for planets around active stars, where stellar activity signatures in RVs can dominate over planetary signatures. As Figure 12 highlights, the number of Neptune-sized planetary systems with precise mass measurements is limited, and detecting and characterizing additional such

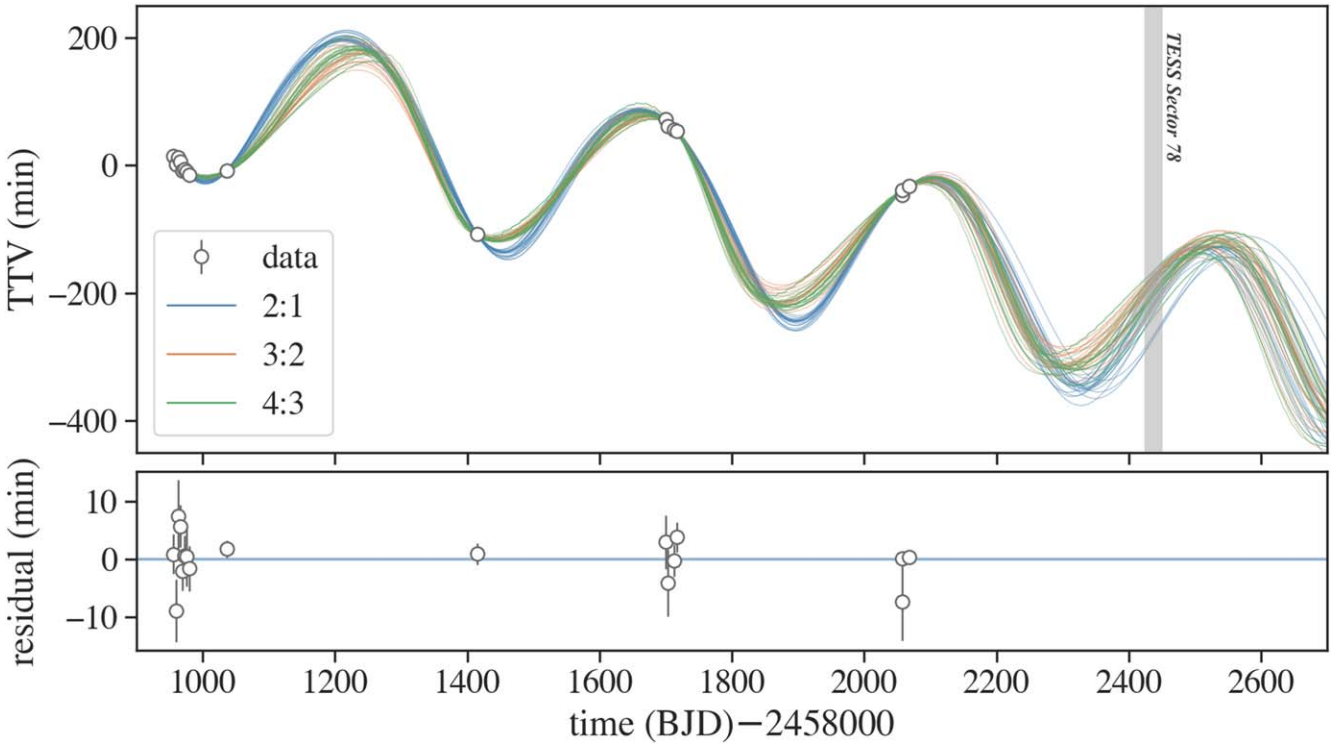

Figure 10. TTVs of TOI-2015 b as a function of time (filled circles). Twenty models corresponding to stable posterior samples from each of the 2:1, 3:2, and 4:3 joint TTV-RV solutions are shown with thin blue, orange, and green lines, respectively. The residuals in the bottom panel are shown with respect to the maximum-likelihood 2:1 solution. Here the TTVs are shown with respect to the ephemeris of t_0(BJD) = 2458956.0238 and $P = 3.3489393$ days obtained by linear fitting of the observed transit times. The linear trend seen in the posterior TTV models in this figure indicates that the mean orbital period inferred from the dynamical modeling differs from the value estimated from the available transit times. TESS will observe TOI-2015 again from 2024 April 23 to 2024 May 21 in Sector 78, denoted by the gray region in the figure.

systems can further aid in understanding the possible bulk and atmospheric compositions of such systems.

5.1.1. Mass Loss and Atmosphere Retention

Given a mass fraction of ∼6% for the H/He envelope, it is useful to estimate if TOI-2015 b could retain its atmosphere as the system evolves. The atmospheres of close-in planets may experience mass loss due to extreme-ultraviolet (EUV) irradiance from their host stars. The intense radiation in the upper atmosphere can facilitate the creation of hydrodynamic winds, resulting in atmospheric escape (Murray-Clay et al. 2009; Salz et al. 2016; Debrecht et al. 2019). To model this photoevaporative process and quantify the potential mass loss TOI-2015 b may experience, we use the following energy-limited mass-loss rate equation from Murray-Clay et al. (2009):

$$\dot{M}_{e\text{-}lim} \sim 6 \times 10^9 \left(\frac{\epsilon}{0.3}\right)\left(\frac{R_p}{10^{10}\ cm}\right)^3 \times \left(\frac{0.7 M_J}{M_p}\right)\left(\frac{F_{EUV}}{450\ erg\ cm^{-2}\ s^{-1}}\right) g\ s^{-1}. \quad (3)$$

Here the *energy-limited* mass loss, $\dot{M}_{\rm e-lim}$, means that essentially all UV radiation received by the planet is used to power photoevaporative winds. ϵ is a heating efficiency factor (see Shematovich et al. 2014). R_p and M_p are planet radius and mass, respectively, and $F_{\rm EUV}$ is the total EUV radiation flux of the host star. To estimate $F_{\rm EUV}$ for TOI-2015, we integrated the Mega-MUSCLES spectrum of GJ 1132, a star that shares TOI-2015's M4 spectral type (Wilson et al. 2021). We specifically calculated the flux in the 300–911.6 Å range of the Mega-MUSCLES EUV spectrum, which is based on an empirical scaling relation using Lyα flux (Linsky et al. 2014).

Assuming values of $\epsilon = 0.3$ (see Murray-Clay et al. 2009) and $F_{\rm EUV} \sim 21\ {\rm erg\ cm^{-2}\ s^{-1}}$ for TOI-2015, we estimate an energy-limited mass-loss rate of $\dot{M}_{\rm e-lim} \sim 6.3 \times 10^7$ g s^{-1} or ∼0.002% Gyr^{-1} given TOI-2015 b's current planetary mass and radius. Using either the gyrochronological age estimate of 1.1 ± 0.1 Gyr or the SED estimate of $6.8^{+4.7}_{-4.6}$ Gyr for the TOI-2015 system, the associated H/He envelope mass fractions of 6.0% and 6.7%, respectively, should be retained with a constant mass-loss rate of $\dot{M}_{\rm e-lim} \sim 0.002\%$ Gyr^{-1}. With this estimate, however, we acknowledge that planets do not experience mass loss at a constant rate over their lifetimes; most mass loss occurs within the first 100 Myr (Owen & Wu 2013).

5.2. Neptune Desert

Figure 13 displays M-dwarf planets in relation to the "Neptune desert," a region around stars where a significant dearth of short-period ($P < \sim$4 days) Neptune-sized planets has been observed (Mazeh et al. 2016). Although the exact causes for the Neptune desert are still debated, the desert could be a relic of orbital migration combined with atmospheric evaporation, where the small, short-period planets we see in the desert were once the cores of Neptunes whose atmospheres were blown away by the intense radiation of their host stars (Owen & Lai 2018).

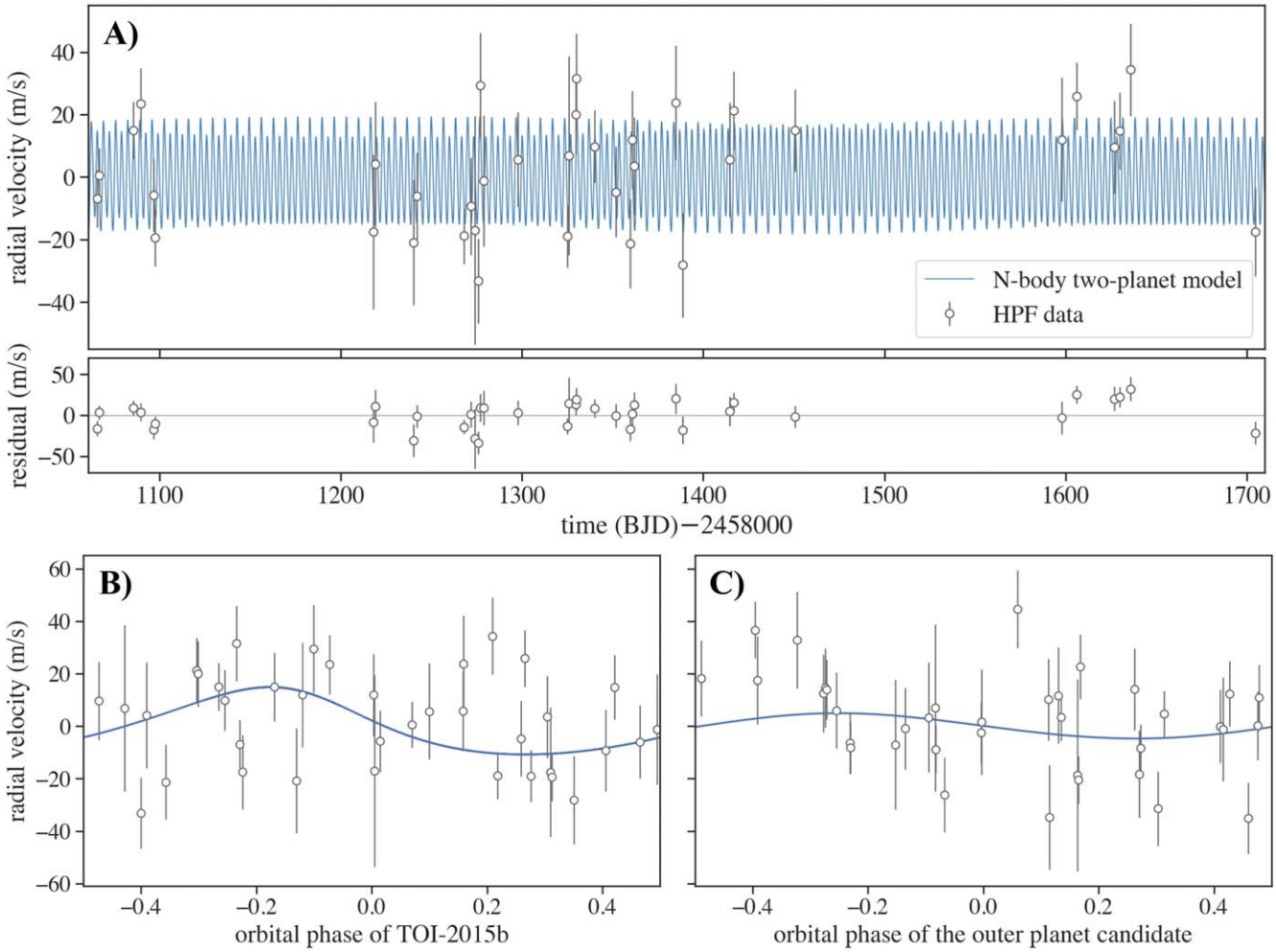

Figure 11. (A) The maximum-likelihood 2:1 solution from the joint TTV and RV fit (blue solid line) compared with the HPF data (white circles with error bars). (B)–(C) The contribution of each planet to the RV signal in the above solution is shown as a function of the orbital phase. Here the signal due to each planet is computed by setting the mass of the other planet to be zero in the *N*-body model. In the right panel, the RV signal due to the inner planet is subtracted from the data. Note that the stellar RVs are computed via direct *N*-body integration in our joint TTV and RV fit, rather than by adding two independent Keplerian signals; thus the RV signals do not have fixed periods in reality.

The Neptune desert is commonly discussed in terms of radius and period. However, recent work has highlighted the role of insolation in shaping the desert and how it varies as a function of stellar type (McDonald et al. 2019; Kanodia et al. 2020, 2021; Powers et al. 2023). The radius–period plane boundaries of the Neptune desert in Mazeh et al. (2016) were defined from observations primarily of FGK stars. To fully understand the landscape of Neptune-sized planets, we must encompass a wider variety of stellar types, including cooler host stars. In radius–insolation space, the boundaries of the desert region are redefined with host star type, taking into account how insolation can vary significantly between planets of similar orbital periods but different spectral classifications (McDonald et al. 2019).

Following Kanodia et al. (2021), we assess TOI-2015 b in relation to the Neptune desert for both period and insolation parameters, plotted in Figure 13. TOI-2015 b falls within the Neptune desert boundary as defined by Mazeh et al. (2016) in period–radius space. However, if we adapt the period boundary into insolation space for FGK stars (which formed the bulk of the host stars in the Mazeh 2016 sample), then TOI-2015 b falls outside of the Neptune desert (dashed line in Figure 13(B)). When we redefine the boundary using the mass and luminosity parameters of an M-dwarf host, we see a less definitive dearth of planets in the region. As such, it is important that we consider radius–insolation space in our study of the Neptune desert for different types of host stars.

5.3. Prospects for Rossiter–McLaughlin Observations

To date, most measurements of stellar obliquity—the angle between the stellar rotation axis and the planet's orbital axis—have been performed for hot Jupiter (HJ) systems, which show a diversity of obliquities from well aligned to highly misaligned orbits (Albrecht et al. 2012, 2022). This has been interpreted as signatures of how HJs form and evolve (Winn & Fabrycky 2015; Albrecht et al. 2022). However, because few small planets—which make up the bulk of known planetary systems—have their obliquity measured, it is unclear if the diverse range of obliquities observed for HJs is tied to the formation process of HJ planets specifically, or if it is a more general outcome of planet formation. As such, increasing the number of smaller planets with obliquity measurements will help yield further clues. Among these, warm Neptunes are particularly interesting, as they orbit far away enough from their stars where tidal forces that could realign them are

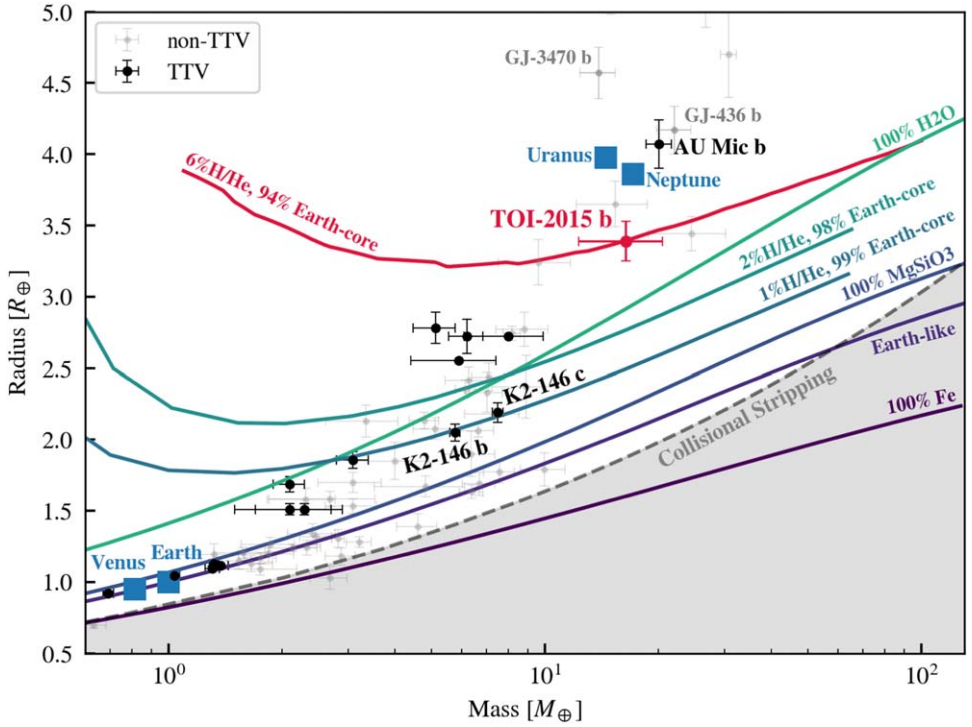

Figure 12. Constraints on the mass and radius of TOI-2015 b. M-dwarf TTV planets are denoted with black points and non-TTV M-dwarf planets are shown with faint gray points. Blue squares show solar system planets. TOI-2015 b (red point) is similar to TTV planets AU Mic b and K2-146 b/c, which have potential composition models consistent with a rocky core and low-mass H/He atmosphere. The red curve shows the two-layer composition model of Lopez & Fortney (2014) with a rocky core shrouded by a H/He envelope, suggesting that TOI-2015 b has a H/He mass fraction of 6%. The other solid lines show composition models from Zeng et al. (2019). The shaded gray region shows where the expected planetary iron content would exceed the maximum value predicted from models of collisional stripping from Marcus et al. (2010).

negligible, making them pristine probes of the original obliquity angle. Interestingly, the few warm Neptunes that have their obliquities constrained around cool stars are observed to show a bifurcation of obliquities (see, e.g., Albrecht et al. 2022; Stefànsson et al. 2022) from well aligned (e.g., K2-25b; Stefansson et al. 2020b) to close to polar (e.g., HAT-P-11b; Winn et al. 2009; GJ 436b, Bourrier et al. 2018; WASP-107b Rubenzahl et al. 2021; GJ 3470b Stefànsson et al. 2022). Further, there is a rising sample of compact multiplanet systems that tend to be well aligned (e.g., Albrecht et al. 2022; Frazier et al. 2023).

The relatively rapid rotation period of the host star and the 1% planet transit depth make TOI-2015 b a promising target for Rossiter–McLaughlin (RM) observations (McLaughlin 1924; Rossiter 1924) to constrain the obliquity of the system. Using $v \sin i = 3.2 \pm 0.6$ km s^{-1} from Table 1 and the radius ratio and impact parameter from Table 2, we use Equation (40) in Winn (2010) to estimate an RM effect amplitude of $\Delta V_{\rm RM} \sim 13$ m s^{-1} for TOI-2015 b. This RM amplitude is similar to the RV semi-amplitude and is within range of the high-precision RV spectrographs on large telescopes that are sensitive in the red-optical or NIR wavelengths such as the Infrared Doppler instrument (Kotani et al. 2014), HPF (Mahadevan et al. 2012, 2014), MAROON-X (Seifahrt et al. 2016, 2020), ESPRESSO (Pepe et al. 2014), and the Keck Planet Finder (Gibson et al. 2016). From the trends observed among Neptunes and multiplanet systems so far, it is possible TOI-2015 b could be well aligned. Obtaining additional obliquities of Neptunes around cool stars, such as TOI-2015 b, will help shed further light into the orbital architectures and the obliquity distribution of close-in Neptune and multiplanet systems.

6. Summary

We report on the discovery of the warm Neptune TOI-2015 b orbiting a nearby ($d = 47$ pc) active M4 dwarf using photometry from the TESS spacecraft, as well as precise photometry from the ground, precise RV observations, and high-contrast imaging. The young host star is active and has a rotation period of $P_{\rm rot} = 8.7 \pm 0.9$ days, and gyrochronological age estimate of 1.1 ± 0.1 Gyr. The planet has an orbital period of $P_{\rm orb} = 3.349$ days, a radius of $R_p = 3.37^{+0.15}_{-0.20}\ R_\oplus$, and a mass of $m_p = 16.4 \pm 4.1 M_\oplus$ from a joint fit of the available photometry and the RVs, resulting in a planet density of $\rho_p = 2.32^{+0.38}_{-0.37}$ g cm^{-3}. These values are compatible with a composition of a rocky planetary core enveloped by a 6% H/He envelope by mass.

The system shows clear TTVs with a super-period $P_{\rm sup} \approx 430$ days and amplitude of $\sim$100 minutes, which we attribute being due to gravitational interactions with an outer planet candidate in the system. We show that the two available sectors of TESS show no evidence of additional transiting planets in the system. We do not see significant evidence for additional planets in the available RVs.

As planets close to period commensurability often show TTVs, to arrive at a mass constraint leveraging both the available RV data and the TTV data we jointly modeled the RVs and the TTVs assuming an outer planet candidate at three likely period commensurabilities of period ratios of 2:1, 3:2, and 4:3 compared to TOI-2015 b. We show that the system is

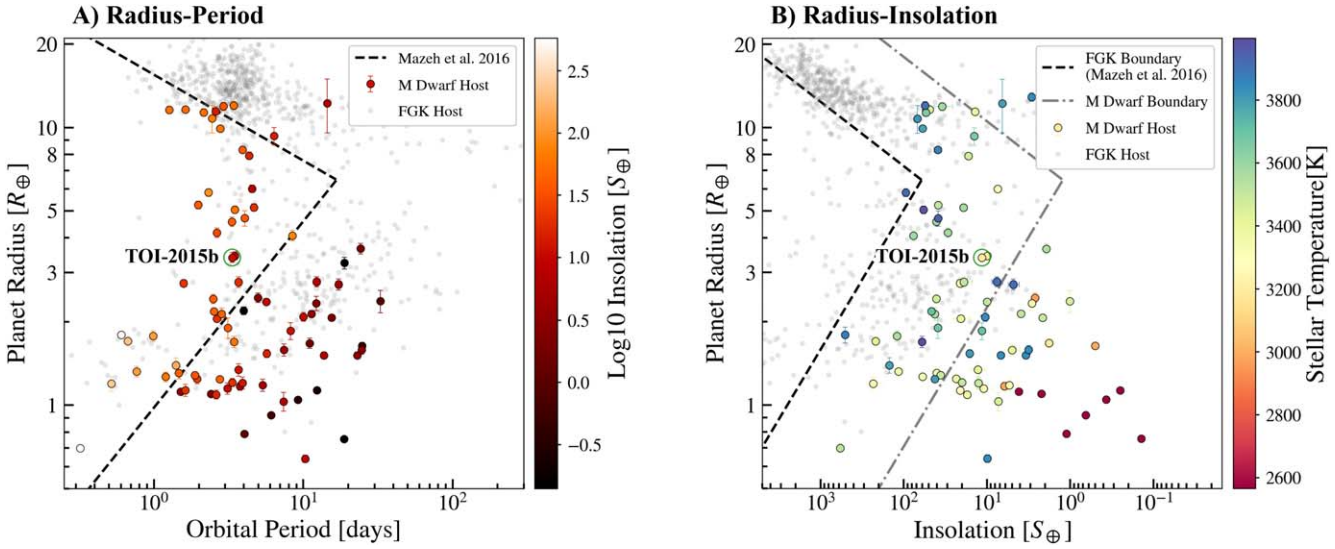

Figure 13. The Neptune desert plotted in radius–period and radius–insolation parameter spaces. Colored points are M-dwarf planets, and translucent gray points are planets with FGK hosts. TOI-2015 b is circled in green. (A) Planet radius vs. orbital period plane. Points are colored by Log10 insolation. The dashed line represents the boundary of the Neptune desert in the radius–period plane as defined by Mazeh et al. (2016). (B) Planet radius vs. insolation plane. Points are colored by stellar effective temperature. The black dashed line represents the Neptune desert boundary as defined by Mazeh et al. (2016), assuming a solar-type star ($M_* = 1\ M_\odot$, $L_* = 1\ L_\odot$). The gray dotted–dashed line is a redefined boundary assuming a M4-type star ($M_* = 0.35\ M_\odot$, $L_* = 0.01\ L_\odot$). While TOI-2015 b falls within the Mazeh et al. (2016) Neptune desert boundary in radius–period space, its host star is a faint red mid-type M dwarf, so the planet receives too little flux to place it inside the Neptune desert.

well described in the 2:1 resonance case, which suggests that TOI-2015 b has a mass of $m_b = 13.3^{+4.7}_{-4.5}\ M_\oplus$—in agreement with the joint transit and RV fit—and that the outer planet candidate has a mass of $m_c = 6.8^{+3.5}_{-2.3}\ M_\oplus$. However, given the data available, other two-planet solutions—including the 3:2 and 4:3 resonance scenarios—cannot be conclusively excluded.

There are a number of characteristics that make TOI-2015 b an interesting target for future studies. TOI-2015 b is one of the most massive known M-dwarf TTV planets, along with AU Mic b. With its large transmission spectroscopy metric of ∼84 (estimated using the equations in Kempton et al. 2018), it is an opportune target for atmospheric observations. This planet is also amenable to constrain obliquity with the RM effect, which would yield further insights into the possible formation history of the system. Most critically, we urge additional transit observations to help further understand the TTVs in the system and characterize the second planet candidate. To aid in future transit observations, we provide predictions of future transit midpoints assuming the 2:1 model is correct in Table 5 in Appendix A3.

Acknowledgments

We thank the reviewer for the thoughtful comments, which helped improve the strength of the manuscript. G.S. acknowledges support provided by NASA through the NASA Hubble Fellowship grant No. HST-HF2-51519.001-A awarded by the Space Telescope Science Institute, which is operated by the Association of Universities for Research in Astronomy, Inc., for NASA, under contract NAS5-26555. This work was partially supported by funding from the Center for Exoplanets and Habitable Worlds. The Center for Exoplanets and Habitable Worlds is supported by the Pennsylvania State University, the Eberly College of Science, and the Pennsylvania Space Grant Consortium. This work was supported by NASA Headquarters under the NASA Earth and Space Science Fellowship Program through grant No. 80NSSC18K1114. We acknowledge support from NSF grants AST-1006676, AST-1126413, AST-1310875, AST-1310885, AST-1517592, AST-1907622, AST-1909506, AST-1910954, AST-2108569, and AST-2108801, the NASA Astrobiology Institute (NAI; grant No. NNA09DA76A), and PSARC in our pursuit of precise radial velocities in the NIR. Computations for this research were performed on the Pennsylvania State University's Institute for Computational & Data Sciences (ICDS). C.I.C. acknowledges support through an appointment to the NASA Postdoctoral Program at the Goddard Space Flight Center administered by ORAU through a contract with NASA. The research was carried out, in part, at the Jet Propulsion Laboratory, California Institute of Technology, under a contract with the National Aeronautics and Space Administration (grant No. 80NM0018D0004).

These results are based on observations obtained with the Habitable-zone Planet Finder Spectrograph on the Hobby–Eberly Telescope. We thank the resident astronomers and telescope operators at the HET for the skillful execution of our observations of our observations with HPF. The Hobby–Eberly Telescope is a joint project of the University of Texas at Austin, the Pennsylvania State University, Ludwig-Maximilians-Universität München, and Georg-August Universität Gottingen. The HET is named in honor of its principal benefactors, William P. Hobby and Robert E. Eberly. The HET collaboration acknowledges the support and resources from the Texas Advanced Computing Center. This work makes use of observations from the Las Cumbres Observatory global telescope network. We acknowledge publicly available data from the LCOGT Key Project (KEY2020B-005), which we retrieved from the LCOGT archive.

Some of the observations in the paper made use of the NN-EXPLORE Exoplanet and Stellar Speckle Imager (NESSI). NESSI was funded by the NASA Exoplanet Exploration Program and the NASA Ames Research Center. NESSI was

built at the Ames Research Center by Steve B. Howell, Nic Scott, Elliott P. Horch, and Emmett Quigley.

We acknowledge the use of public TOI release data from pipelines at the TESS Science Office and at the TESS Science Processing Operations Center. This research has made use of the Exoplanet Follow-up Observation Program website, which is operated by the California Institute of Technology, under contract with the National Aeronautics and Space Administration under the Exoplanet Exploration Program. This paper includes data collected by the TESS mission, which are publicly available from the Multimission Archive for Space Telescopes (MAST). Support for MAST for non-HST data is provided by the NASA Office of Space Science via grant No. NNX09AF08G and by other grants and contracts. This research made use of the SIMBAD database, operated at CDS, Strasbourg, France. This research made use of `lightkurve`, a Python package for Kepler and TESS data analysis (Lightkurve Collaboration et al. 2018). This research made use of the NASA Exoplanet Archive, which is operated by the California Institute of Technology, under contract with the National Aeronautics and Space Administration under the Exoplanet Exploration Program. This work has made use of data from the European Space Agency (ESA) mission Gaia (https://www.cosmos.esa.int/gaia), processed by the Gaia Data Processing and Analysis Consortium (DPAC; https://www.cosmos.esa.int/web/gaia/dpac/consortium). Funding for the DPAC has been provided by national institutions, in particular the institutions participating in the Gaia Multilateral Agreement.

Facilities: TESS, Gaia, HET (HPF), WIYN (NESSI), Shane (ShARCS), SSO:1m, WIRO, RBO, ARC (ARCTIC).

Software: `AstroImageJ` (Collins et al. 2017), `astroplan` (Morris et al. 2018), `astropy` (Astropy Collaboration et al. 2013), `astroquery` (Ginsburg et al. 2018), `barycorrpy` (Kanodia & Wright 2018), `batman` (Kreidberg 2015), `corner.py` (Foreman-Mackey 2016), `celerite` (Foreman-Mackey et al. 2017), `dynesty` (Speagle 2020), `EXOFASTv2` (Eastman 2017), `GALPY` (Bovy 2015), `GNU Parallel` (Tange 2011), `HxRGproc` (Ninan et al. 2018), `iDiffuse` (Stefansson et al. 2018b), `jnkepler` (K. Masuda 2024, in preparation), `Jupyter` (Kluyver et al. 2016), `juliet` (Espinoza et al. 2019), `matplotlib` (Hunter 2007), `MultiNest` (Feroz et al. 2009; Buchner et al. 2014), `numpy` (Van Der Walt et al. 2011), `pandas` (McKinney 2010), `radvel` (Fulton et al. 2018), `SERVAL` (Zechmeister et al. 2018), `transitleastsquares` (Hippke & Heller 2019), `TTVFast` (Deck et al. 2014).

Appendix A
Transiting Exoplanet Survey Satellite Photometry and Future Transits

A.1. Individual TESS Transits

Figure 14 shows each individual transit from TESS Sectors 24 and 51, accounting for the TTVs.

A.2. Transit Timing Variations

Table 4 shows the TTV midpoint time for each transit observation used in this study with their transit numbers from the first observed TESS transit (transit 0).

A.3. Future Predicted Transits

Table 5 lists future predicted transits assuming the near 2:1 resonance solution.

A.4. Corner Plot of 2:1 Solution

Figure 15 shows a corner plot of the posteriors from the 2:1 solution.

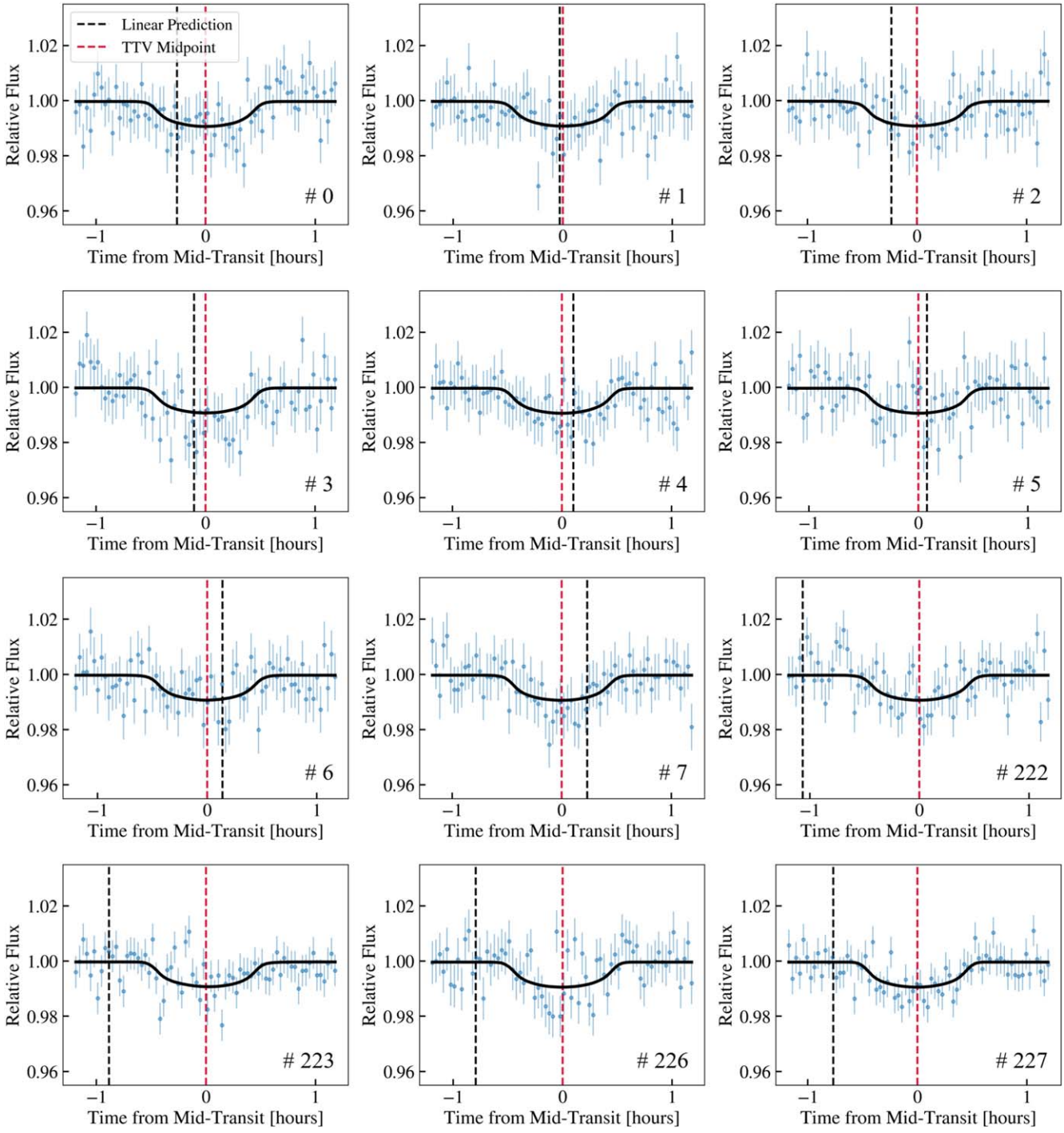

Figure 14. Individual TESS transits detrended photometry with `juliet` TTV fit model. The vertical black lines represent the expected linear predictions, and the vertical red lines are the true TTV midpoints. Transit number is labeled in the bottom-right corner of each transit.

Table 4
TTV Midpoints from `juliet` Joint Fit

Instrument	Transit Number	TTV (BJD)
TESS	0	$2458956.0335^{+0.0025}_{-0.0026}$
TESS	1	$2458959.3727^{+0.0038}_{-0.0033}$
TESS	2	$2458962.7303^{+0.0039}_{-0.0049}$
TESS	3	$2458966.0739^{+0.0029}_{-0.0026}$
TESS	4	$2458969.4141^{+0.0023}_{-0.0023}$
TESS	5	$2458972.7641^{+0.0026}_{-0.0026}$
TESS	6	$2458976.1106^{+0.0034}_{-0.0039}$
TESS	7	$2458979.4557^{+0.0028}_{-0.0026}$
LCOGT	24	$2459036.3923^{+0.0011}_{-0.0011}$
WIRO	137	$2459414.7537^{+0.0012}_{-0.0014}$
TESS	222	$2459699.5379^{+0.0030}_{-0.0036}$
TESS	223	$2459702.8793^{+0.0043}_{-0.0023}$
TESS	226	$2459712.9224^{+0.0019}_{-0.0020}$
TESS	227	$2459716.2703^{+0.0017}_{-0.0018}$
RBO	329	$2460057.7924^{+0.0045}_{-0.0044}$
ARC	329	$2460057.7974^{+0.00043}_{-0.00044}$
ARC	332	$2460067.8488^{+0.00037}_{-0.00036}$

Note. Instruments/facilities: Transiting Exoplanet Survey Satellite (TESS), Las Cumbres Observatory Global Telescope (LCOGT), Wyoming Infrared Observatory (WIRO), Red Buttes Observatory (RBO), Astrophysical Research Council (ARC).

Table 5
Predicted Future Mid-transit Times of TOI-2015 b and Their Uncertainties for the 2:1 Solution

Predicted Transit Midpoint (UTC)	Predicted Transit Midpoint (BJD)	Midpoint Uncertainty (days)
2024-08-04 01:56:38	2460526.581	0.021
2024-08-07 10:17:46	2460529.929	0.021
2024-08-10 18:40:19	2460533.278	0.021
2024-08-14 03:01:26	2460536.626	0.021
2024-08-17 11:22:34	2460539.974	0.021
…	…	…

Notes. The values shown are the mean and standard deviation calculated from the stable posterior samples derived in Section 4.3. We note that the transits could happen ∼100 minutes later than these values if the 3:2 or 4:3 solutions are correct. Only the first five entries are shown here; the full table is available online.

(This table is available in its entirety in machine-readable form in the online article.)

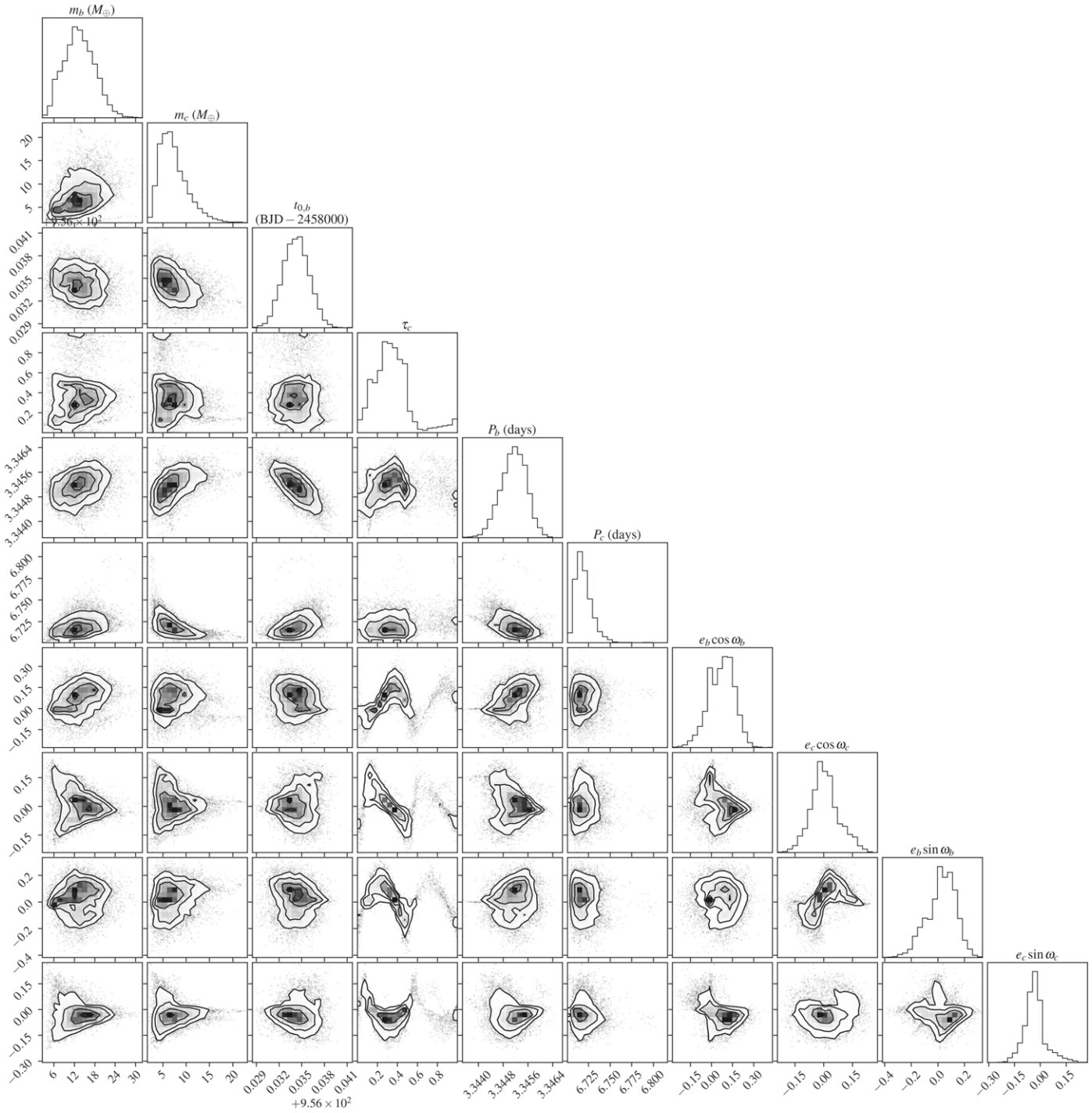

Figure 15. Corner plot for the stable posterior samples from the joint TTV-RV fit assuming the 2:1 period ratio. The figure was created using `corner.py` (Foreman-Mackey 2016).

Appendix B
Habitable-zone Planet Finder Radial Velocities and Activity Indicators

Table 6 lists the RVs from HPF and associated activity indicators derived from the HPF spectra used in this work.

Table 6
HPF RVs Used in This Work Along with the Differential Line Width (dLW), Chromatic Index (CRX), and the Line Indices for the Three Ca II Infrared Triplet Lines (Ca II IRT 1, 2 and 3), Along with Associated Errors

BJD	RV ($m\ s^{-1}$)	dLW ($m^2\ s^{-2}$)	CRX ($m\ s^{-1}\ Np^{-1}$)	Ca II IRT 1	Ca II IRT 2	Ca II IRT 3
2459065.674261	-6.9 ± 9.2	63.3 ± 24.3	61.3 ± 99.1	0.815 ± 0.006	0.548 ± 0.006	0.505 ± 0.005
2459066.671994	0.6 ± 8.7	63.2 ± 23.1	164.0 ± 110.5	0.832 ± 0.006	0.555 ± 0.006	0.513 ± 0.005
2459085.624486	15.0 ± 9.1	38.6 ± 24.4	202.5 ± 114.3	0.856 ± 0.006	0.547 ± 0.006	0.510 ± 0.005
2459089.613160	23.5 ± 11.3	-18.1 ± 30.4	48.2 ± 118.3	…	0.629 ± 0.009	0.584 ± 0.007
2459096.599695	-5.7 ± 11.7	58.1 ± 31.4	-75.4 ± 157.7	0.852 ± 0.008	0.570 ± 0.009	0.516 ± 0.007
2459097.596633	-19.4 ± 9.1	36.0 ± 24.5	-134.3 ± 88.7	1.105 ± 0.007	0.781 ± 0.007	0.695 ± 0.006
2459218.030657	-17.6 ± 24.7	-60.5 ± 67.3	555.4 ± 235.5	0.932 ± 0.021	0.629 ± 0.021	0.539 ± 0.019
2459219.032663	4.1 ± 20.1	22.3 ± 54.2	199.1 ± 243.6	0.905 ± 0.016	0.621 ± 0.017	0.557 ± 0.014
2459239.973718	-20.9 ± 20.0	-148.7 ± 54.8	89.4 ± 248.5	0.818 ± 0.016	0.517 ± 0.017	0.514 ± 0.014
2459241.967614	-6.1 ± 13.9	32.0 ± 37.5	-264.6 ± 227.0	0.793 ± 0.010	0.522 ± 0.010	0.491 ± 0.008
2459267.907011	-18.8 ± 8.9	15.2 ± 23.9	-86.9 ± 121.1	0.843 ± 0.006	0.541 ± 0.006	0.497 ± 0.005
2459271.881308	-9.3 ± 15.6	71.4 ± 41.8	-21.5 ± 194.2	0.968 ± 0.012	0.638 ± 0.011	0.597 ± 0.010
2459273.885647	-17.0 ± 36.5	-160.4 ± 100.3	-241.4 ± 362.9	0.838 ± 0.027	0.503 ± 0.030	0.418 ± 0.027
2459275.875276	-33.2 ± 13.6	-59.7 ± 36.9	-91.5 ± 111.3	0.785 ± 0.010	0.519 ± 0.010	0.496 ± 0.008
2459276.877445	29.4 ± 16.8	-16.9 ± 45.5	315.8 ± 173.6	…	0.524 ± 0.012	0.506 ± 0.010
2459278.870972	-1.2 ± 21.0	16.9 ± 56.7	-53.6 ± 238.2	0.836 ± 0.015	0.538 ± 0.017	0.515 ± 0.015
2459297.817717	5.7 ± 15.1	85.2 ± 40.4	-100.2 ± 227.0	0.907 ± 0.012	0.577 ± 0.012	0.520 ± 0.010
2459324.975199	-19.0 ± 9.8	90.9 ± 26.1	-139.2 ± 129.2	0.871 ± 0.007	0.596 ± 0.007	0.555 ± 0.005
2459325.963842	6.8 ± 31.8	96.6 ± 84.2	-485.4 ± 277.7	0.854 ± 0.025	0.684 ± 0.025	0.579 ± 0.020
2459329.735950	19.9 ± 12.6	5.9 ± 33.5	236.5 ± 154.5	0.805 ± 0.009	0.561 ± 0.009	0.508 ± 0.007
2459329.958065	31.5 ± 14.4	74.0 ± 38.2	10.5 ± 162.5	0.816 ± 0.010	0.583 ± 0.011	0.531 ± 0.008
2459339.929512	9.8 ± 11.6	68.8 ± 30.7	140.7 ± 136.6	0.850 ± 0.008	0.574 ± 0.008	0.536 ± 0.006
2459351.683197	-4.8 ± 14.5	-50.3 ± 39.3	-157.3 ± 177.3	…	0.566 ± 0.011	0.506 ± 0.008
2459359.659352	-21.3 ± 14.3	-46.9 ± 38.2	55.5 ± 171.3	0.886 ± 0.010	0.615 ± 0.010	0.561 ± 0.008
2459360.866097	11.9 ± 15.6	33.5 ± 41.6	342.8 ± 220.5	0.838 ± 0.010	0.574 ± 0.011	0.541 ± 0.009
2459361.873109	3.5 ± 15.6	-52.2 ± 41.8	36.0 ± 101.3	0.849 ± 0.011	0.560 ± 0.011	0.490 ± 0.009
2459384.805438	23.8 ± 18.3	96.1 ± 48.7	-374.0 ± 305.1	0.979 ± 0.013	0.602 ± 0.014	0.582 ± 0.011
2459388.793553	-28.1 ± 16.7	-27.0 ± 45.2	201.6 ± 223.2	0.955 ± 0.012	0.647 ± 0.013	0.537 ± 0.010
2459414.718289	5.6 ± 18.3	-85.2 ± 49.3	-151.4 ± 167.7	0.895 ± 0.012	0.566 ± 0.013	0.523 ± 0.010
2459416.714349	21.2 ± 12.5	-59.4 ± 33.5	31.9 ± 151.2	0.914 ± 0.008	0.598 ± 0.008	0.560 ± 0.007
2459450.621745	15.0 ± 13.1	4.6 ± 35.1	-14.3 ± 92.4	0.908 ± 0.009	0.574 ± 0.009	0.584 ± 0.007
2459597.992508	11.9 ± 19.9	-20.4 ± 53.3	80.8 ± 230.4	0.862 ± 0.013	0.559 ± 0.013	0.522 ± 0.011
2459605.972370	25.8 ± 10.8	110.7 ± 28.8	44.3 ± 124.4	…	0.542 ± 0.007	0.524 ± 0.006
2459626.920928	9.6 ± 14.9	14.7 ± 40.2	-151.6 ± 214.0	0.797 ± 0.009	0.496 ± 0.009	0.481 ± 0.009
2459629.913211	14.8 ± 12.3	-56.2 ± 33.4	-97.5 ± 147.7	0.921 ± 0.008	0.579 ± 0.008	0.567 ± 0.007
2459635.896290	34.3 ± 14.8	-118.8 ± 40.2	-1.8 ± 154.9	0.840 ± 0.010	0.544 ± 0.011	0.515 ± 0.009
2459704.703361	-17.5 ± 14.1	281.2 ± 37.0	53.4 ± 167.1	0.863 ± 0.010	0.572 ± 0.009	0.550 ± 0.008

(This table is available in its entirety in machine-readable form in the online article.)

ORCID iDs

Sinclaire E. Jones https://orcid.org/0000-0002-7227-2334
Guðmundur Stefánsson https://orcid.org/0000-0001-7409-5688
Kento Masuda https://orcid.org/0000-0003-1298-9699
Jessica E. Libby-Roberts https://orcid.org/0000-0002-2990-7613
Cristilyn N. Gardner https://orcid.org/0000-0001-8621-6731
Rae Holcomb https://orcid.org/0000-0002-5034-9476
Corey Beard https://orcid.org/0000-0001-7708-2364
Paul Robertson https://orcid.org/0000-0003-0149-9678
Caleb I. Cañas https://orcid.org/0000-0003-4835-0619
Suvrath Mahadevan https://orcid.org/0000-0001-9596-7983
Shubham Kanodia https://orcid.org/0000-0001-8401-4300
Andrea S. J. Lin https://orcid.org/0000-0002-9082-6337
Henry A. Kobulnicky https://orcid.org/0000-0002-4475-4176
Brock A. Parker https://orcid.org/0000-0001-9307-8170
Chad F. Bender https://orcid.org/0000-0003-4384-7220
William D. Cochran https://orcid.org/0000-0001-9662-3496
Scott A. Diddams https://orcid.org/0000-0002-2144-0764
Rachel B. Fernandes https://orcid.org/0000-0002-3853-7327
Arvind F. Gupta https://orcid.org/0000-0002-5463-9980
Samuel Halverson https://orcid.org/0000-0003-1312-9391
Suzanne L. Hawley https://orcid.org/0000-0002-6629-4182
Fred R. Hearty https://orcid.org/0000-0002-1664-3102
Leslie Hebb https://orcid.org/0000-0003-1263-8637
Adam Kowalski https://orcid.org/0000-0001-7458-1176
Jack Lubin https://orcid.org/0000-0001-8342-7736
Andrew Monson https://orcid.org/0000-0002-0048-2586
Joe P. Ninan https://orcid.org/0000-0001-8720-5612
Lawrence Ramsey https://orcid.org/0000-0002-4289-7958
Arpita Roy https://orcid.org/0000-0001-8127-5775
Christian Schwab https://orcid.org/0000-0002-4046-987X
Ryan C. Terrien https://orcid.org/0000-0002-4788-8858
John Wisniewski https://orcid.org/0000-0001-9209-1808

References

Agol, E., Hernandez, D. M., & Langford, Z. 2021, MNRAS, 507, 1582
Agol, E., Steffen, J., Sari, R., & Clarkson, W. 2005, MNRAS, 359, 567
Albrecht, S., Winn, J. N., Johnson, J. A., et al. 2012, ApJ, 757, 18

Albrecht, S. H., Dawson, R. I., & Winn, J. N. 2022, PASP, 134, 082001
Astropy Collaboration, Robitaille, T. P., Tollerud, E. J., et al. 2013, A&A, 558, A33
Bailer-Jones, C. A. L., Rybizki, J., Fouesneau, M., Demleitner, M., & Andrae, R. 2021, AJ, 161, 147
Baraffe, I., & Chabrier, G. 2018, A&A, 619, A177
Barros, S. C. C., Díaz, R. F., Santerne, A., et al. 2014, A&A, 561, L1
Betancourt, M. 2017, arXiv:1701.02434
Bingham, E., Chen, J. P., Jankowiak, M., et al. 2019, JMLR, 20, 1
Bourrier, V., Lecavelier des Etangs, A., Ehrenreich, D., Tanaka, Y. A., & Vidotto, A. A. 2016, A&A, 591, A121
Bourrier, V., Lovis, C., Beust, H., et al. 2018, Natur, 553, 477
Bovy, J. 2015, ApJS, 216, 29
Bradbury, J., Frostig, R., Hawkins, P., et al. 2018, JAX: Composable Transformations of Python+NumPy programs, v0.3.13, GitHub, https://github.com/google/jax
Brown, T. M., Baliber, N., Bianco, F. B., et al. 2013, PASP, 125, 1031
Bryant, E. M., Bayliss, D., & Van Eylen, V. 2023, MNRAS, 521, 3663
Buchner, J., Georgakakis, A., Nandra, K., et al. 2014, A&A, 564, A125
Carrillo, A., Hawkins, K., Bowler, B. P., Cochran, W., & Vanderburg, A. 2020, MNRAS, 491, 4365
Cifuentes, C., Caballero, J. A., Cortés-Contreras, M., et al. 2020, A&A, 642, A115
Collins, K. A., Kielkopf, J. F., Stassun, K. G., & Hessman, F. V. 2017, AJ, 153, 77
Cresswell, P., & Nelson, R. P. 2006, A&A, 450, 833
Cutri, R. M., Skrutskie, M. F., van Dyk, S., et al. 2003, The IRSA 2MASS All-Sky Point Source Catalog, NASA/IPAC Infrared Science Archive, http://irsa.ipac.caltech.edu/applications/Gator/
Cutri, R. M., Wright, E. L., & Conrow, T. 2021, yCat, II/328
Dai, F., Masuda, K., Beard, C., et al. 2023, AJ, 165, 33
Debrecht, A., Carroll-Nellenback, J., Frank, A., et al. 2019, MNRAS, 483, 1481
Deck, K. M., Agol, E., Holman, M. J., & Nesvorný, D. 2014, ApJ, 787, 132
Dressing, C. D., & Charbonneau, D. 2015, ApJ, 807, 45
Duane, S., Kennedy, A., Pendleton, B. J., & Roweth, D. 1987, PhLB, 195, 216
Eastman, J. 2017, EXOFASTv2: Generalized Publication-quality Exoplanet Modeling Code, Astrophysics Source Code Library, ascl:1710.003
Eastman, J. D., Rodriguez, J. E., Agol, E., et al. 2019, arXiv:1907.09480
Engle, S. G., & Guinan, E. F. 2023, ApJL, 954, L50
Espinoza, N. 2018, RNAAS, 2, 209
Espinoza, N., Kossakowski, D., & Brahm, R. 2019, MNRAS, 490, 2262
Feiden, G. A., Skidmore, K., & Jao, W.-C. 2021, ApJ, 907, 53
Feroz, F., Hobson, M. P., & Bridges, M. 2009, MNRAS, 398, 1601
Findlay, J. R., Kobulnicky, H. A., Weger, J. S., et al. 2016, PASP, 128, 115003
Foreman-Mackey, D. 2016, JOSS, 1, 24
Foreman-Mackey, D. 2018, RNAAS, 2, 31
Foreman-Mackey, D., Agol, E., Ambikasaran, S., & Angus, R. 2017, AJ, 154, 220
Frazier, R. C., Stefánsson, G., Mahadevan, S., et al. 2023, ApJL, 944, L41
Fulton, B. J., Petigura, E. A., Blunt, S., & Sinukoff, E. 2018, PASP, 130, 044504
Gagné, J., Mamajek, E. E., Malo, L., et al. 2018, ApJ, 856, 23
Gaia Collaboration, Vallenari, A., Brown, A. G. A., et al. 2023, A&A, 674, A1
Gan, T., Wang, S. X., Wang, S., et al. 2023, AJ, 165, 17
Gardner-Watkins, C. N., Kobulnicky, H. A., Jang-Condell, H., et al. 2023, AJ, 165, 5
Gavel, D., Kupke, R., Dillon, D., et al. 2014, Proc. SPIE, 9148, 914805
Gelman, A., Carlin, J. B., Stern, H. S., et al. 2014, Bayesian Data Analysis (3rd ed.; Boca Raton, FL: CRC Press)
Gibson, S. R., Howard, A. W., Marcy, G. W., et al. 2016, Proc. SPIE, 9908, 2093
Gillon, M., Jehin, E., Lederer, S. M., et al. 2016, Natur, 533, 221
Gillon, M., Triaud, A. H. M. J., Demory, B.-O., et al. 2017, Natur, 542, 456
Ginsburg, A., Sipocz, B., Parikh, M., et al. 2018, astropy/astroquery: v0.3.7, Zenodo, doi:10.5281/zenodo.1160627
Hamann, A., Montet, B. T., Fabrycky, D. C., Agol, E., & Kruse, E. 2019, AJ, 158, 133
Hardegree-Ullman, K. K., Cushing, M. C., Muirhead, P. S., & Christiansen, J. L. 2019, AJ, 158, 75
Hedges, C., Angus, R., Barentsen, G., et al. 2020, RNAAS, 4, 220
Henden, A. A., Levine, S., Terrell, D., & Welch, D. L. 2015, AAS Meeting, 225, 336.16
Henry, T. J., Jao, W.-C., Subasavage, J. P., et al. 2006, AJ, 132, 2360
Hippke, M., & Heller, R. 2019, A&A, 623, A39
Hirano, T., Dai, F., Gandolfi, D., et al. 2018, AJ, 155, 127
Holman, M. J., & Murray, N. W. 2005, Sci, 307, 1288
Howell, S. B., Everett, M. E., Sherry, W., Horch, E., & Ciardi, D. R. 2011, AJ, 142, 19
Howell, S. B., Sobeck, C., Haas, M., et al. 2014, PASP, 126, 398
Huehnerhoff, J., Ketzeback, W., Bradley, A., et al. 2016, Proc. SPIE, 9908, 99085H
Hunter, J. D. 2007, CSE, 9, 90
Jao, W.-C., Henry, T. J., Gies, D. R., & Hambly, N. C. 2018, ApJL, 861, L11
Kanodia, S., Cañas, C. I., Stefansson, G., et al. 2020, ApJ, 899, 29
Kanodia, S., Mahadevan, S., Ramsey, L. W., et al. 2018, Proc. SPIE, 10702, 107026Q
Kanodia, S., Stefansson, G., Cañas, C. I., et al. 2021, AJ, 162, 135
Kanodia, S., & Wright, J. 2018, RNAAS, 2, 4
Kaplan, K. F., Bender, C. F., Terrien, R., et al. 2018, in ASP. Conf. Ser. 523, Astronomical Data Analysis Software and Systems XXVIII, ed. P. J. Teuben et al. (San Francisco, CA: ASP), 567
Kasper, D. H., Ellis, T. G., Yeigh, R. R., et al. 2016, PASP, 128, 105005
Kempton, E. M. R., Bean, J. L., Louie, D. R., et al. 2018, PASP, 130, 114401
Kipping, D. M. 2013, MNRAS, 435, 2152
Kluyver, T., Ragan-Kelley, B., Pérez, F., et al. 2016, in Positioning and Power in Academic Publishing: Players, Agents and Agendas, ed. B. Schmidt & F. Loizides (Amsterdam: IOS Press), 87
Kotani, T., Tamura, M., Suto, H., et al. 2014, Proc. SPIE, 9147, 914714
Kreidberg, L. 2015, PASP, 127, 1161
Kumar, S. S. 1963, ApJ, 137, 1121
Lam, K. W. F., Korth, J., Masuda, K., et al. 2020, AJ, 159, 120
Laughlin, G., Bodenheimer, P., & Adams, F. C. 1997, ApJ, 482, 420
Lépine, S., Hilton, E. J., Mann, A. W., et al. 2013, AJ, 145, 102
Li, J., Tenenbaum, P., Twicken, J. D., et al. 2019, PASP, 131, 024506
Lightkurve Collaboration, Cardoso, J. V. d. M., Hedges, C., et al. 2018, Lightkurve: Kepler and TESS Time Series Analysis in Python, Astrophysics Source Code Library, ascl:1812.013
Limber, D. N. 1958, ApJ, 127, 363
Linsky, J. L., Fontenla, J., & France, K. 2014, ApJ, 780, 61
Lithwick, Y., Xie, J., & Wu, Y. 2012, ApJ, 761, 122
Lopez, E. D., & Fortney, J. J. 2014, ApJ, 792, 1
Mahadevan, S., Ramsey, L., Bender, C., et al. 2012, Proc. SPIE, 8446, 84461S
Mahadevan, S., Ramsey, L. W., Terrien, R., et al. 2014, Proc. SPIE, 9147, 91471G
Marcus, R. A., Sasselov, D., Hernquist, L., & Stewart, S. T. 2010, ApJL, 712, L73
Martioli, E., Hébrard, G., Correia, A. C. M., Laskar, J., & Lecavelier des Etangs, A. 2021, A&A, 649, A177
Masci, F. J., Laher, R. R., Rusholme, B., et al. 2019, PASP, 131, 018003
Masset, F., & Snellgrove, M. 2001, MNRAS, 320, L55
Masuda, K. 2017, AJ, 154, 64
Masuda, K., & Winn, J. N. 2020, AJ, 159, 81
Mazeh, T., Holczer, T., & Faigler, S. 2016, A&A, 589, A75
McCully, C., Turner, M., Volgenau, N., et al. 2018, LCOGT/banzai: Initial Release v0.9.4, Zenodo, doi:10.5281/zenodo.1257560
McDonald, G. D., Kreidberg, L., & Lopez, E. 2019, ApJ, 876, 22
McKinney, W. 2010, in Proc. 9th Python in Science Conf., ed. S. van der Walt & J. Millman (Austin, TX: SciPy), 51
McLaughlin, D. B. 1924, ApJ, 60, 22
Ment, K., & Charbonneau, D. 2023, AJ, 165, 265
Metcalf, A. J., Anderson, T., Bender, C. F., et al. 2019, Optic, 6, 233
Monson, A. J., Beaton, R. L., Scowcroft, V., et al. 2017, AJ, 153, 96
Morris, B. M., Tollerud, E., Sipőcz, B., et al. 2018, AJ, 155, 128
Muirhead, P. S., Dressing, C. D., Mann, A. W., et al. 2018, AJ, 155, 180
Muirhead, P. S., Mann, A. W., Vanderburg, A., et al. 2015, ApJ, 801, 18
Murray-Clay, R. A., Chiang, E. I., & Murray, N. 2009, ApJ, 693, 23
Nesvorný, D., Kipping, D., Terrell, D., et al. 2013, ApJ, 777, 3
Newton, E. R., Charbonneau, D., Irwin, J., et al. 2014, AJ, 147, 20
Newton, E. R., Irwin, J., Charbonneau, D., et al. 2017, ApJ, 834, 85
Ninan, J. P., Bender, C. F., Mahadevan, S., et al. 2018, Proc. SPIE, 10709, 107092U
Ninan, J. P., Stefansson, G., Mahadevan, S., et al. 2020, ApJ, 894, 97
Owen, J. E., & Lai, D. 2018, MNRAS, 479, 5012
Owen, J. E., & Wu, Y. 2013, ApJ, 775, 105
Paegert, M., Stassun, K. G., Collins, K. A., et al. 2021, arXiv:2108.04778
Pepe, F., Molaro, P., Cristiani, S., et al. 2014, AN, 335, 8
Phan, D., Pradhan, N., & Jankowiak, M. 2019, arXiv:1912.11554
Plavchan, P., Barclay, T., Gagné, J., et al. 2020, Natur, 582, 497
Powers, L. C., Libby-Roberts, J., Lin, A. S. J., et al. 2023, AJ, 166, 44
Rein, H., Hernandez, D. M., Tamayo, D., et al. 2019, MNRAS, 485, 5490
Rein, H., & Liu, S. F. 2012, A&A, 537, A128

Ricker, G. R., Winn, J. N., Vanderspek, R., et al. 2015, JATIS, 1, 014003
Robertson, P., Mahadevan, S., Endl, M., & Roy, A. 2014, Sci, 345, 440
Rossiter, R. A. 1924, ApJ, 60, 15
Rubenzahl, R. A., Dai, F., Howard, A. W., et al. 2021, AJ, 161, 119
Salz, M., Czesla, S., Schneider, P. C., & Schmitt, J. H. M. M. 2016, A&A, 586, A75
Scott, N. J., Howell, S. B., Horch, E. P., & Everett, M. E. 2018, PASP, 130, 054502
Seifahrt, A., Bean, J. L., Stürmer, J., et al. 2016, Proc. SPIE, 9908, 990818
Seifahrt, A., Bean, J. L., Stürmer, J., et al. 2020, Proc. SPIE, 11447, 114471F
Shematovich, V. I., Ionov, D. E., & Lammer, H. 2014, A&A, 571, A94
Shetrone, M., Cornell, M. E., Fowler, J. R., et al. 2007, PASP, 119, 556
Smith, J. C., Stumpe, M. C., Cleve, J. E. V., et al. 2012, PASP, 124, 1000
Snellgrove, M. D., Papaloizou, J. C. B., & Nelson, R. P. 2001, A&A, 374, 1092
Speagle, J. S. 2020, MNRAS, 493, 3132
Stassun, K. G., Oelkers, R. J., Paegert, M., et al. 2019, AJ, 158, 138
Stassun, K. G., Oelkers, R. J., Pepper, J., et al. 2018, AJ, 156, 102
Stefansson, G., Cañas, C., Wisniewski, J., et al. 2020a, AJ, 159, 100
Stefansson, G., Hearty, F., Robertson, P., et al. 2016, ApJ, 833, 175
Stefansson, G., Li, Y., Mahadevan, S., et al. 2018a, AJ, 156, 266
Stefansson, G., Mahadevan, S., Hebb, L., et al. 2017, ApJ, 848, 9
Stefansson, G., Mahadevan, S., Maney, M., et al. 2020b, AJ, 160, 192
Stefànsson, G., Mahadevan, S., Petrovich, C., et al. 2022, ApJL, 931, L15
Stefansson, G., Mahadevan, S., Wisniewski, J., et al. 2018b, Proc. SPIE, 10702, 1070250
Stumpe, M. C., Smith, J. C., Catanzarite, J. H., et al. 2014, PASP, 126, 100
Tange, O. 2011, login: The USENIX Magazine, Zenodo, doi:10.5281/zenodo.16303
Twicken, J. D., Catanzarite, J. H., Clarke, B. D., et al. 2018, PASP, 130, 064502
Van Der Walt, S., Colbert, S. C., & Varoquaux, G. 2011, CSE, 13, 22
West, A. A., Weisenburger, K. L., Irwin, J., et al. 2015, ApJ, 812, 3
Wilson, D. J., Froning, C. S., Duvvuri, G. M., et al. 2021, ApJ, 911, 18
Winn, J. 2010, in Exoplanets (Space Science Series) Vol. 526, ed. S. Seager (Tucson, AZ: Univ. Arizona Press), 55
Winn, J. N., & Fabrycky, D. C. 2015, ARA&A, 53, 409
Winn, J. N., Johnson, J. A., Albrecht, S., et al. 2009, ApJL, 703, L99
Wright, J. T., & Eastman, J. D. 2014, PASP, 126, 838
Zechmeister, M., & Kürster, M. 2009, A&A, 496, 577
Zechmeister, M., Reiners, A., Amado, P. J., et al. 2018, A&A, 609, A12
Zeng, L., Jacobsen, S. B., Sasselov, D. D., et al. 2019, PNAS, 116, 9723